

TENSOR NETWORK METHODS FOR
INFINITE 2D SYSTEMS

MARC ZIEGLER



JOHANNES GUTENBERG
UNIVERSITÄT MAINZ

A Study of the Heisenberg Quantum Antiferromagnet on the Kagome Lattice

April 2015

Marc Ziegler: *Tensor Network Methods for infinite 2D systems*, A Study of the Heisenberg Quantum Antiferromagnet on the Kagome Lattice, © April 2015

SUPERVISORS:

Jun.-Prof. Román Orús

Jun.-Prof. Matteo Rizzi

DECLARATION

Ich versichere, dass ich die Arbeit selbstständig verfasst und keine anderen als die angegebenen Quellen und Hilfsmittel benutzt sowie Zitate kenntlich gemacht habe.

Mainz, April 2015

Marc Ziegler

Marc Ziegler
Johannes Gutenberg-Universität D-55099 Mainz
Institut für Physik
Komet337
Staudingerweg 7
mziegle@students.uni-mainz.de

ABSTRACT

One of the great challenges in modern-day physics is to determine the properties of quantum many-body systems. In particular, we try to describe macroscopic systems by their fundamental microscopic interactions. Currently, we still lack the tools to tackle this task in a general fashion since even simple Hamiltonians give rise to very complex and strongly correlated behaviour of the system.

Since we are only able to describe very few systems analytically, we utilise numerical techniques to determine the properties of many-body systems. Exact numerical methods, like *exact diagonalization*, suffer from the problem that the Hilbert space of a system scales exponentially with its size. Thus, efficient numerical approximations are needed to describe large systems. In recent years, many of these numerical techniques have been developed, e.g. *quantum Monte Carlo* or *series expansion*. However, there are still systems which are very hard to manage. Systems with very strong correlations and geometric frustration are amongst the hardest problems and many methods fail in describing these systems.

Here we focus on a rather new numerical method which is based on the tensor network description of a quantum many-body system. This method exploits the fact, that the ground states of short-ranged Hamiltonians lie in a low-entanglement region of the corresponding Hilbert space. Tensor network states have the useful property that they lie in this region by construction and therefore have been shown to be a very useful tool to represent the low-energy states of local Hamiltonians.

In this thesis we will first explain the used iPEPS algorithm which is based on the *projected entangled pair states* (PEPS) ansatz for many-body systems. This algorithm can be used to calculate the ground state properties of quantum systems on infinite two-dimensional lattices. Afterwards we will benchmark this algorithm with well-known and well studied systems, and then use it to tackle models which are as of now not fully understood. Specifically, we will deal with the Heisenberg model on the kagome lattice. This model has been analysed with many different techniques but still faces many important challenges. We will investigate this spin model for different spin values, and will provide legitimate results where other methods failed.

ZUSAMMENFASSUNG

Eine große Herausforderung in der modernen Physik ist es, die Eigenschaften von quantenmechanischen Vielteilchensystemen zu bestimmen. Dabei versucht man, makroskopische Systeme durch ihre fundamentalen mikroskopischen Wechselwirkungen vollständig zu beschreiben. Momentan fehlen jedoch die passenden Werkzeuge, um solch ein Problem im Allgemeinen zu lösen, da selbst einfache Hamiltonoperatoren sehr komplexes und stark korreliertes Verhalten hervorbringen. Da nur sehr wenige Systeme eine analytische Beschreibung zulassen, nutzen wir numerische Techniken, um die Eigenschaften von Vielteilchensystemen zu bestimmen. Exakte numerische Methoden, wie *Exakte Diagonalisierung* des Hamiltonoperators, leiden unter dem Problem, dass der Hilbertraum des Systems exponentiell mit der Systemgröße anwächst. Daher benötigt man effiziente numerische Approximationen, um große Systeme zu beschreiben. In den letzten Jahrzehnten wurden viele numerische Methoden entwickelt, wie z.B. *Quanten-Monte-Carlo*. Leider gibt es immer noch Systeme die nur schwer für einige dieser Methoden zugänglich sind. Besonders Systeme mit starken Korrelationen und geometrischer Frustration gehören zu den schwersten Problemen, da viele Methoden es nicht schaffen, solche Systeme korrekt zu beschreiben.

In dieser Arbeit legen wir unser Augenmerk auf eine eher neue numerische Methode, welche auf der Beschreibung des Quantenzustandes durch Tensor-Netzwerke basiert. Diese Methode nutzt aus, dass der Grundzustand lokaler Hamiltonoperatoren in einem Bereich geringer Verschränkung des Hilbertraums liegt. Tensor-Netzwerk-Zustände haben die intrinsische Eigenschaft genau in diesem Bereich zu liegen und sind deshalb sehr nützlich um Grundzustände lokaler Hamiltonoperatoren darzustellen.

In dieser Arbeit erklären wir zuerst den verwendeten iPEPS-Algorithmus, welcher auf dem *projected entangled pair states* (PEPS)-Ansatz für Vielteilchensysteme basiert. Dieser Algorithmus eignet sich sehr gut zum Berechnen der Grundzustandseigenschaften von zweidimensionalen Quanten-Gitter-Systemen. Anschließend werden wir den Algorithmus mit Hilfe gut bekannter und ausführlich studierter Modelle benchmarken, bevor wir ihn zur Untersuchung weniger bekannter Modelle benutzen. Dabei handelt es sich um das Heisenberg-Modell auf dem Kagome-Gitter mit verschiedenen Spinwerten, welches zwar bereits mit vielen Methoden angegangen wurde, aber noch nicht vollkommen verstanden ist. Deshalb versuchen wir, schlüssige Ergebnisse mit unseren Methoden dort zu erzielen, wo andere Methoden versagt haben.

ACKNOWLEDGMENTS

First of all I would like to thank my supervisor Jun.-Prof. Román Orús for all his help, his suggestions, and his guidance and his continuous trust in me and my abilities. Furthermore I want to thank Jun.-Prof. Matteo Rizzi for many fruitful discussions.

Additionally I want to thank all my colleagues within our group for all the lunch and coffee breaks. Without these this year working on my thesis would not have been this much fun. Especially I want to thank Johannes, Augustine and Kai for making all the time spend in the office very enjoyable.

Of course I also like to thank all my friends and my volleyball club for giving me a very nice balance to the every day life at the university.

Most of all I would like to thank Elena Sips for her love, support and inspiration. Last but not least I would like to thank my parents and my sister for all their love and support throughout all my studies.

CONTENTS

I INTRODUCTION AND THEORY	1
1 INTRODUCTION	3
2 BASIC CONCEPTS	5
2.1 Entanglement	5
2.2 Quantum Phase Transitions	6
2.3 Singular Value Decomposition	7
2.4 Variational principle	8
3 TENSOR NETWORKS	11
3.1 Why Tensor Networks	11
3.2 Diagrammatic Notation	12
3.3 Tensor Network description of Quantum States	14
3.4 Area-law in Tensor Network States	15
3.5 Numerical TN methods for infinite PEPS	17
3.5.1 Finding the ground state	17
3.5.2 Simple Update	19
3.5.3 Calculating expectation values	21
3.5.4 Computational Complexity	25
II BENCHMARKING OF THE CODE	27
4 THE 2D CLASSICAL ISING MODEL	29
4.1 The Model	29
4.2 Results	29
5 THE 2D QUANTUM ISING MODEL	35
5.1 The Model	35
5.2 Results	36
III THE HEISENBERG MODEL ON THE KAGOME LATTICE	41
6 INTRODUCTION	43
7 THE SPIN- $1/2$ KAGOME HEISENBERG ANTIFERROMAGNET	45
7.1 Mapping to the square lattice	46
7.2 Ground State Energy	47
7.3 Nature of the ground state	52
7.4 KAFM with a magnetic field	54

8	THE SPIN-1 KAGOME HEISENBERG ANTIFERROMAGNET	59
8.1	Ground state energy	60
8.2	Nature of the Ground State	63
8.3	Spin-1 KAFM with a Magnetic Field	64
9	THE SPIN- $3/2$ KAGOME HEISENBERG ANTIFERROMAGNET	67
9.1	Gound State Energy	68
9.2	Nature of the Ground State	70
9.3	Spin- $3/2$ KAFM with a Magnetic Field	71
10	CONCLUSION	75
	IV APPENDIX	81
A	APPENDIX	83
A.1	The full update	83
A.2	CTM for a 2×2 unit cell	84
A.3	Different mapping from the Kagome to the square lattice	85
	BIBLIOGRAPHY	87

LIST OF FIGURES

Figure 3.1	Area-law of the entanglement entropy	12
Figure 3.2	Relevant corner of the Hilbert space	12
Figure 3.3	Basic tensor network diagrams	13
Figure 3.4	Example for a simple tensor network	13
Figure 3.5	Trace written as a tensor network	13
Figure 3.6	TN representation (MPS) of a quantum state	14
Figure 3.7	Examples for TN quantum states	15
Figure 3.8	Entanglement between subsystems in a PEPS	16
Figure 3.9	Imaginary time evolution written as a TN	18
Figure 3.10	PEPS with a 2x2 unit cell and translational invariance	19
Figure 3.11	TN diagram for the simple update	20
Figure 3.12	TN for calculating expectation values	21
Figure 3.13	Corner transfer matrices for the 2D plane	21
Figure 3.14	CTM algorithm	22
Figure 3.15	Expectation value of some one-site observable	23
Figure 3.16	HOTRG algorithm	25
Figure 4.1	Partition function of the 2D classical Ising model written as a TN	30
Figure 4.2	Expectation value for the classical Ising as the ratio of two TN	31
Figure 4.3	Magnetization per site in the 2D classical Ising model	31
Figure 4.4	Calculating the correlation function	32
Figure 4.5	Spin-Spin correlator for the classical Ising model	32
Figure 5.1	Magnetization and ground state energy for the quantum Ising model	36
Figure 5.2	Magnetization of the quantum Ising model around the critical field	37
Figure 5.3	Jump in the first order phase transition for the quantum Ising model	38
Figure 5.4	Comparison of the CTM and HOTRG algorithm	39
Figure 5.5	The difference between the expectation values obtained by the CTM and HOTRG algorithm	39
Figure 6.1	Kagome lattice	43
Figure 6.2	Graphical representation of the frustration within a triangular lattice	44
Figure 6.3	Japanese kagome basket	44
Figure 7.1	Mapping scheme from the kagome to the square lattice	47
Figure 7.2	Convergence of E_0 depending on χ	48

Figure 7.3	Scaling of E_0 to infinite bond dimension	50
Figure 7.4	Comparison of our results with other methods	51
Figure 7.5	Bond strength map of the KAFM for different bond dimensions of the PEPS	53
Figure 7.6	Energy difference in the bond strength map	54
Figure 7.7	Magnetization curve of the kagome Heisenberg antiferromagnet	55
Figure 7.8	Bond strength map within the magnetization plateau	56
Figure 8.1	Trimerization within the kagome lattice	59
Figure 8.2	Scaling to an infinite bond dimension from the obtained data	61
Figure 8.3	Comparison of the results obtained by our method and the results of other methods.	62
Figure 8.4	Energy of each link in the kagome lattice	64
Figure 8.5	Magnetization curve of the spin-1 KAFM	65
Figure 9.1	Scaling towards infinite bond dimension for the spin- $3/2$ KAFM	69
Figure 9.2	Comparison of the ground state energies of the spin- $3/2$ KAFM obtained by different methods.	70
Figure 9.3	Bond strength map of the ground state of the spin- $3/2$ antiferromagnet.	71
Figure 9.4	Magnetization curve of the spin- $3/2$ KAFM	72
Figure 9.5	Bond strength map of the spin- $3/2$ KAFM within the plateau of the magnetization curve	73
Figure 10.1	Behaviour of the ground state energy depending on the spin of the Heisenberg model	77
Figure A.1	Starting points of the full update	83
Figure A.2	Distance between two TN quantum states	84
Figure A.3	CTM algorithm	85
Figure A.4	Alternate mapping from the kagome to the square lattice	86

LIST OF TABLES

Table 3.1	Computational cost	26
Table 7.1	Ground state energies of the spin-1/2 Heisenberg model on the kagome lattice.	49
Table 8.1	Ground state energies per lattice site for the spin 1 heisenberg model on the kagome lattice.	60
Table 9.1	Ground state energy of the spin-3/2 antiferromagnet on the kagome lattice	68
Table 10.1	Summary of all results obtained in this thesis	76

ACRONYMS

CTM	corner transfer matrix
PEPS	projected entangled pair state
MPS	matrix product state
HOTRG	higher order tensor renormalization group
TN	tensor network
SVD	singular value decomposition
HOSVD	higher order singular value decomposition
QSL	quantum spin liquid
VBC	valence bond crystal

Part I

INTRODUCTION AND THEORY

INTRODUCTION

Even with all the advances in computational science and the larger amounts of computational resources available today, it is still a challenging problem to determine the properties of a quantum many-body system. A better understanding of such systems would give rise to great advances in many other fields, like material science, condensed matter physics and quantum field theory. However, it is very hard to treat such large systems since the complexity scales exponentially with the number of particles.

This makes it incredibly hard to calculate the properties of a macroscopic ensemble of many particles from the microscopic description of the individual components. Due to this problem, Feynman suggested in 1982 [18] that one should put the peculiarities of quantum mechanics to good use by exploiting these properties to simulate complex quantum systems with other quantum systems, which are simpler and easier to control. This method would be exponentially faster compared to the calculations with a classical Turing machine. Hence people have been trying to build a quantum simulator of reasonable size to simulate such systems for many years.

This proposition was intriguing not only from an experimental point of view, but also from a theoretical one. It gave rise to a completely new field of physics: quantum information. In the early beginnings of this field, it mostly took advantage from the results and methods which were known from other fields. However, over time completely new methods were developed within the context of quantum information which are now finding application in many other fields like quantum chemistry or even string theory[55].

The reason for this is the fact, that quantum information has developed a detailed study of quantum entanglement which is a purely quantum property without any classical analogy. It describes the correlation between parts of a quantum system. It is a measure of how the measurement of one part influences the measurement of the other one. Because of this correlation, which does not have to be local, entanglement was very controversial at the beginnings of quantum mechanics. Einstein called it a “spooky interaction” and formulated together with Podolsky and Rosen the so-called EPR-paradox[15] because they were not able to accept the concept of non-locality. This paradox should show that quantum mechanics was incomplete and some physics was still missing which would be accounted for by some missing variables. To settle this question, Bell[3] derived some inequalities which, when tested experimentally, would verify if hidden variables exist or quantum me-

chanics is complete. The following experiments [2] showed that the Bell inequalities are violated, which means that entanglement is real and quantum mechanics is complete.

Entanglement is a very useful tool which can be used to find ground states of many-body systems. The reason for this, is that the ground states of gapped, local Hamiltonians lie in a low-entanglement region of the Hilbert space. This means that we only need to consider a very small subspace of the enormous Hilbert space to find the ground state of a given Hamiltonian. Thus, it would be very useful to find a representation of the quantum state which is systematically confined to this low entanglement region. Such a representation is given by *tensor networks* (TNs), which were developed quite recently as an ansatz for quantum states of many-body systems with limited amounts of entanglement. The most well-known TN ansatz for a quantum state is the so called *matrix product state* (MPS).

During the development of the TN ansatz, White[59] developed a variational method to find the ground state of certain systems based on the methods from renormalization group. This method is known as *density matrix renormalization group* (DMRG). Shortly afterwards it was noticed that the DMRG algorithm could be expressed in the MPS formalism. All of this gave rise to a lot of different methods and algorithms to determine the quantum states of many-body systems, e.g. time-evolving block decimation (TEBD).

In this thesis, we will use some of these methods which are based on TNs to find the ground states of two dimensional systems. All the algorithms which are used in this thesis are based on the *projected entangled pair states* (PEPS) ansatz. This ansatz is the natural extension of the one-dimensional MPS ansatz to two dimensions.

We will first give a short introduction into the important physical and mathematical concepts (chapter 2) and then continue to introduce tensor networks and the algorithms used in this thesis based on them (chapter 3). We will describe how to obtain ground state approximations as well as expectation values for infinite two dimensional translationally invariant lattices based on the PEPS ansatz. In Part II we will study some well-known models to give a benchmark of the performance of the algorithms. Once this benchmark is established, we will study the Heisenberg model on the kagome lattice, which is still topic to a lot of discussions, and show that PEPS can be used to investigate the properties of highly frustrated systems (see Part III).

BASIC CONCEPTS

2.1 ENTANGLEMENT

Einstein described entanglement as a “spooky interaction” at a distance [15]. It describes a correlation between two systems which only exists on a quantum level. Imagine these two systems span the Hilbert spaces \mathcal{H}_1 and \mathcal{H}_2 . We say these two systems are entangled if the wave function $|\psi\rangle \in \mathcal{H}_1 \otimes \mathcal{H}_2$ of the complete system cannot be written as a product of pure states of the two Hilbert spaces:

$$|\psi\rangle_{12} \neq |\varphi\rangle_1 \otimes |\chi\rangle_2 \quad \text{with} \quad |\varphi\rangle_1 \in \mathcal{H}_1, |\chi\rangle_2 \in \mathcal{H}_2 \quad (2.1)$$

An example for such an entangled state is the state $|\psi^+\rangle_{12}$ which is given by

$$|\psi^+\rangle_{12} = \frac{1}{\sqrt{2}} (|0\rangle_1 |0\rangle_2 + |1\rangle_1 |1\rangle_2). \quad (2.2)$$

This non-locality, which is implied by quantum mechanics, was the subject to a lot of discussion and scepticism and the so-called hidden variable models (HVM) were created which did not have this implied non-locality. To test between these different models, Bell[3] formulated the so called Bell-inequalities. If they are violated, the HVM must be untrue and only a non-local theory can describe nature. In 1982 the violation of the Bell-inequalities was experimentally shown[2] and thus the HVM were proven to be incorrect and entanglement must be a part of reality.

Nowadays entanglement is not only seen as a quantum mechanical effect but also as a useful resource. With the help of entanglement it is, e.g. possible to construct schemes for quantum teleportation. This was first proposed in [4] in 1993 and later proven experimentally[6]. With the help of quantum teleportation it would be possible to construct quantum repeaters which can be used to build a quantum information network over the world giving rise to new forms of quantum encrypted forms of communication [10, 16]. It is also possible to perform a quantum teleportation over great distances. The longest distance achieved for a teleportation so far is over 143 km between two Canary Islands [35]. It is however not only possible to teleport the state of a single particle over a long distance, but also to teleport the quantum state of a macroscopic ensemble [31].

A second use for entanglement is in the context of quantum computation. The elementary unit which is needed for quantum computation, the so called *qubit*, is a two-level-system. For the algorithms, which can

be used with quantum computers, a highly entangled state of many qubits is needed. Therefore entanglement is the key element in all the algorithms for quantum computation.

2.2 QUANTUM PHASE TRANSITIONS ¹

Consider a Hamiltonian $\mathcal{H}(g)$ which is defined on a certain lattice and varies as a function of some dimensionless coupling g . We identify any point of non-analyticity in the ground state energy at $g = g_c$ with a phase transition. This non-analyticity can occur due to e.g. level crossing of the energy bands.

We are mainly interested in *second-order phase transitions*, which occur if the energy gap

$$\Delta = E_1(g) - E_0(g) \quad (2.3)$$

between the ground state and the first excited state vanishes at $g = g_c$. For this kind of phase transitions one finds in most cases that, as g approaches g_c , Δ vanishes as

$$\Delta \sim J|g - g_c|^\beta \quad (2.4)$$

where β is also known as the critical exponent of the gap. This exponent is *universal*, which means that it is independent of most of the details of the Hamiltonian.

However, not only the energy gap vanishes, but also the correlation length in the system diverges at $g = g_c$ in a very similar fashion and one finds that

$$\Delta \propto \xi^{-z} \quad (2.5)$$

where z is also known as *dynamic critical exponent*.

To determine g_c one usually does not have to calculate Δ itself, but it is enough to calculate some local order parameter m which is $m = 0$ on one side of g_c and $m \neq 0$ on the other side. The point where this value turns to zero is the phase transition point g_c .

Such phase transitions are usually also accompanied by a change of the symmetries in the system. The phase with a non-zero order parameter has less symmetries than the phase where the order parameter vanishes. This theory of phase transitions with a change of symmetries is known as *Landau's theory of phase transitions*.

It is a very general concept in many-body physics and also particle physics that ground states often exhibit a phenomenon called *spontaneous symmetry breaking*. This means that the ground state itself lacks certain symmetries which are present in the underlying Hamiltonian. As examples of this symmetry breaking one can give the Ising model,

¹ This chapter is based on [52]

the Heisenberg model or, according to particle physics, the whole universe.²

There are however phases of matter which go beyond this theory of spontaneous symmetry breaking. Landau's theory is a classical theory and does not describe quantum mechanical effects. Quantum mechanics however implies new kinds of orders due to non-local effects, which go beyond Landau's paradigm. Phases which have such a non-local behaviour also exist in nature as the ground states of quantum many-body systems. These systems can exhibit long-range quantum entanglement and develop topological order. This is a very non-local order which is defined by topological features of the ground state. Such topological phases usually have a robust ground state degeneracy which means that the different ground states cannot change into each other under local perturbations. Due to these non-local properties it is not possible to describe topological phases with the Landau theory and therefore are of great interest. There are many proposals to use these ground states to build topologically protected qubits for quantum computation which would be stable against local perturbations [13]. With this it would be possible to construct quantum computers which can run at finite temperatures and do not need to operate near $T = 0$ K.

2.3 SINGULAR VALUE DECOMPOSITION

The *singular value decomposition* of a matrix describes the representation through the product of three specific matrices. It is similar to the well-known eigenvalue decomposition of a matrix, but with slightly different properties.

The singular value decomposition of a complex $m \times n$ -matrix M is given by the product

$$M = U\Sigma V^\dagger \quad (2.6)$$

where

U is an isometric $m \times m$ -matrix ($U^\dagger U = \mathbb{1}$)

V^\dagger is the adjoint of an isometric $n \times n$ -matrix ($V^\dagger V = \mathbb{1}$)

Σ is a real diagonal $m \times n$ -matrix.

The matrix Σ has $r \leq \min(m, n)$ positive real entries on its diagonal, the so called singular values of M . These are uniquely determined by M (though the matrices U and V are not). Thus Σ has the form

² The Ising and Heisenberg model will be explained in more detail later in this thesis.

$$\Sigma = \left(\begin{array}{ccc|ccc} \lambda_1 & & & & \vdots & \\ & \ddots & & \dots & 0 & \dots \\ & & \lambda_r & & \vdots & \\ \hline & \vdots & & & \vdots & \\ \dots & 0 & \dots & \dots & 0 & \dots \\ & \vdots & & & \vdots & \end{array} \right) \quad (2.7)$$

where $\lambda_1 \geq \dots \geq \lambda_r > 0$.

To calculate the singular values one can use the property

$$M^\dagger M = (V\Sigma U^\dagger) \cdot (U\Sigma V^\dagger) = V\Sigma\Sigma V^\dagger \quad (2.8)$$

which means that the singular values equal the square root of the eigenvalues of $M^\dagger M$.

Since the singular values can be arranged in a descending order within Σ , this decomposition is sometimes used for truncating schemes within tensor network algorithms (see sec. 3.5).

2.4 VARIATIONAL PRINCIPLE

Suppose we have a certain Hamiltonian \mathcal{H} with a discrete spectrum (to avoid complications about continuous spectra). From this we can write the eigenvalue equation

$$\hat{\mathcal{H}}|\psi_E\rangle = E|\psi_E\rangle \quad (2.9)$$

and from the spectral theorem we know that

$$\sum_{E_i \in \text{Spec}(\mathcal{H})} |\psi_{E_i}\rangle \langle \psi_{E_i}| = \mathbb{1}. \quad (2.10)$$

With these properties we want to determine the lower bound of the expectation value of \mathcal{H} with any quantum state $|\Psi\rangle$. We can write the expectation value as

$$\langle \Psi | \mathcal{H} | \Psi \rangle = \sum_{E_i, E_j \in \text{Spec}(\mathcal{H})} \langle \Psi | \psi_{E_i} \rangle \langle \psi_{E_i} | \mathcal{H} | \psi_{E_j} \rangle \langle \psi_{E_j} | \Psi \rangle \quad (2.11)$$

$$= \sum_{E_i \in \text{Spec}(\mathcal{H})} E_i |\langle \psi_{E_i} | \Psi \rangle|^2 \quad (2.12)$$

$$\geq \sum_{E_i \in \text{Spec}(\mathcal{H})} E_0 |\langle \psi_{E_i} | \Psi \rangle|^2 = E_0. \quad (2.13)$$

Hence E_0 represents a lower bound to the expectation value of \mathcal{H} . We can therefore find an upper bound to the ground state energy by searching for the state $|\varphi\rangle$ out of a certain set of states that gives the infimum of the expectation value of \mathcal{H} :

$$E_0 \leq \frac{\langle \varphi | \mathcal{H} | \varphi \rangle}{\langle \varphi | \varphi \rangle} \quad \forall |\varphi\rangle. \quad (2.14)$$

By this principle, we can give upper bounds to the ground state energy by approximating the ground state with numerical methods and search for the approximated one with the lowest expectation value of the ground state energy.

3.1 WHY TENSOR NETWORKS

Tensor networks have proven very useful as a numerical and analytical tool to understand the properties of quantum many-body systems, especially strongly correlated systems. But since the amount of existing numerical methods is quite large, one may wonder about the advantages of tensor networks.

Every numerical technique has its own limitations. Quantum Monte Carlo [39] has the sign problem, which restricts its usage for e.g. frustrated quantum spin systems; exact diagonalization of the Hamiltonian [12] can only be used for rather small systems; series expansion [42] suffers from the limits of perturbation theory, etc. Of course TN methods do also have their limitations, but this limit is quite different from the ones mentioned above: the restriction is the amount of entanglement in the system. Therefore TNs can be used to simulate new models and explore new directions.

The Hilbert space of a quantum many-body system is very large. For example, if you have a spin-1/2-system with N particles, the dimension of the Hilbert space is 2^N . This means that the Hilbert space grows exponentially with the number of particles in the system. Consider now a typical physical many-body system, which is common in a lab, with $N \sim 10^{23}$ (of the order of the Avogadro number). Thereby it follows that the Hilbert space dimension is $\sim \mathcal{O}(10^{10^{23}})$, which is incredibly large (the amount of atoms in the observable universe is estimated to be $\sim 10^{80}$).

However not all states in the Hilbert space are equally relevant for us. In nature it is found that the interaction between particles tends to be local. One can show that the corresponding ground states of gapped Hamiltonians with local interaction obey the so-called *area law* for the entanglement entropy [11]. This means that the entanglement entropy of a subsystem does not scale with the volume of the subsystem but with its boundary (fig. 3.1). For an arbitrary state this is not given which means that this area-law constraints the states which are relevant for us.

Therefore the low-energy states of these Hamiltonians describe only a very small, in fact exponentially small, corner of the Hilbert space (see fig. 3.2). The advantage of TN states is that they obey the area-law by construction. That means that they target directly the relevant corner of the Hilbert space. However it has recently been shown that

¹ This chapter is based on [46]

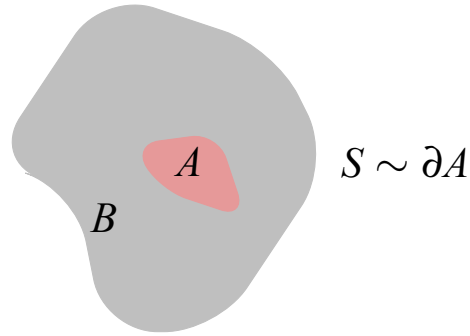


Figure 3.1: The entanglement entropy S of a subsystem A in B scales with the boundary ∂A between A and B

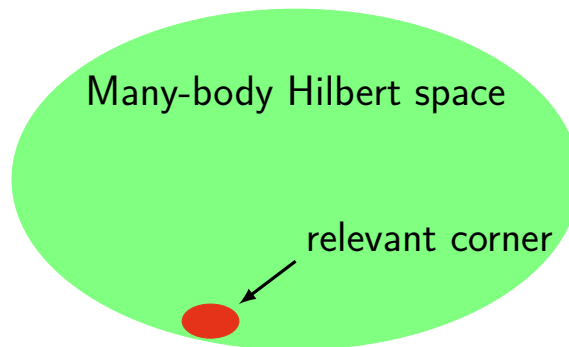


Figure 3.2: The relevant states of the Hilbert space which obey the area law describe only a very small part of the large space of all states.

not every state in this area-law obeying region can be approximated with TN states in the case of two or more dimensions[20]. However the states, that cannot be approximated by TNs, are not eigenstates of local Hamiltonians either and therefore not very relevant for the systems we are interested in. This makes TN a very powerful tool since there is no need to be concerned with the complete Hilbert space, but only with the states which lie in the relevant corner.

3.2 DIAGRAMMATIC NOTATION

This section will give an introduction to some of the mathematical concepts which are used in TN methods. We will also define what a TN state is, what TN diagrams are and how quantum states can be represented by these.

A tensor is a multi-dimensional array of complex coefficients. The *rank* of such a tensor is given by the number of its indices. These tensors can also be represented graphically in terms of *tensor network diagrams* (fig. 3.3). The contraction over an index is given by the sum over all

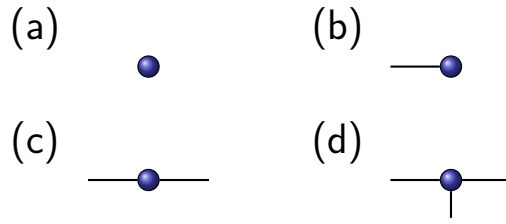


Figure 3.3: Tensor network diagrams of (a) scalar, (b) vector, (c) matrix and (d) rank-3 tensor

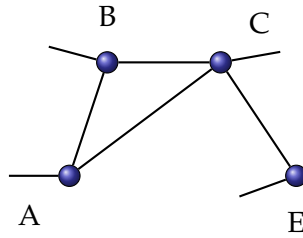


Figure 3.4: Tensor Network diagram of equation 3.2. It is a contraction of 4 tensors and 4 open indices.

the values of the shared indices of a set of tensors. This means that the normal matrix product

$$C_{\alpha\beta} = \sum_{\gamma=1}^{D_\gamma} A_{\alpha\gamma} B_{\gamma\beta} \tag{3.1}$$

is the contraction over the shared index γ . Of course one can always think of more complicated contractions like

$$F_{\alpha\beta\gamma\delta} = \sum_{\eta}^{D_\eta} \sum_{\sigma}^{D_\sigma} \sum_{\epsilon}^{D_\epsilon} \sum_{\lambda}^{D_\lambda} A_{\alpha\eta\epsilon} B_{\eta\sigma\beta} C_{\sigma\gamma\epsilon\lambda} E_{\lambda\delta}. \tag{3.2}$$

Equation (3.2) can also be written as a tensor network diagram which can be seen in figure 3.4. This TN diagram representation allows us to handle the rather complicated equation (3.2) in a nice visual way. However it is not only better to handle but one can also see some properties, which are not that obvious within the corresponding equations. For example, the cyclic properties of the trace can easily be seen in the tensor network diagram (see fig. 3.5).

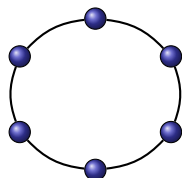


Figure 3.5: Trace of product of 6 matrices. One can see directly the cyclic properties of the trace.

3.3 TENSOR NETWORK DESCRIPTION OF QUANTUM STATES

Now that the basic ideas of tensor networks are explained, let us see how they can be used to describe quantum states of many-body systems. For that we consider a system which contains N particles within a d -level system. Thus, the wave function can be written in the individual basis of the single particles $|i_r\rangle$ ($i_r = 1, \dots, d$) and takes the general form

$$|\psi\rangle = \sum_{i_1} \sum_{i_2} \cdots \sum_{i_N} C_{i_1 i_2 \cdots i_N} |i_1\rangle |i_2\rangle \cdots |i_N\rangle. \quad (3.3)$$

The coefficients $C_{i_1 i_2 \cdots i_N}$ can be seen as entries in a large N -legged tensor C . This is a very big tensor with $\mathcal{O}(d^N)$ entries and rank N . For computational purposes this is a very inefficient description of the quantum state, but with the help of TN states one can reduce the complexity by giving an accurate description of the entanglement properties of the state. Therefore one decomposes this one big tensor into a TN of many smaller tensors with a smaller rank (see fig. 3.6).



Figure 3.6: The representation of the coefficients of a quantum state through a tensor network. This particular form of a TN is a so-called matrix product state (MPS)

This new TN representation of the quantum state $|\psi\rangle$ is a more efficient description from a computational point of view. The amount of parameters does no longer scale exponentially, but rather polynomial in the number of particles.

To determine the number of parameters n_{tot} , one has to first think about the number of parameters per tensor T . This is given by

$$n(t) = \mathcal{O} \left(\prod_{\alpha_T}^{rank(T)} D(\alpha_T) \right), \quad (3.4)$$

where the product runs over all indices $\alpha_T = 1, \dots, rank(T)$ of T , and $D(\alpha_T)$ is the size of the dimension which is corresponding to α_T .

If the maximum of $D(\alpha_T)$ is given by D_T then this $n(t)$ is given by

$$n(t) = \mathcal{O} \left(D_T^{rank(T)} \right). \quad (3.5)$$

This is the amount of parameters per tensor in the TN. Thus the total amount of parameters is

$$n_{tot} = \sum_{T=1}^{N_{TN}} n(T), \quad (3.6)$$

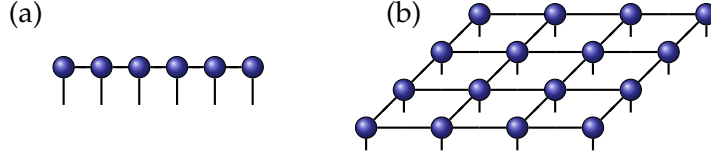


Figure 3.7: Simple examples for a TN description of a quantum state. (a) matrix product state (MPS) with periodic boundary conditions (b) projected entangled pair state (PEPS) with open boundary conditions

where N_{TN} is the amount of tensors T in the TN. This amount needs to be less than exponential in N to be useful for computational purposes. This means that $N_{TN} = \mathcal{O}(\text{poly}(N))$ and if we combine all this we get

$$n_{tot} = \mathcal{O}(\text{poly}(N)\text{poly}(D)), \quad (3.7)$$

where D is the maximum of all D_T and we assume that the rank of each tensor has an upper bound.

Simple examples for such a TN description of a quantum state can be seen in fig. 3.7. However this efficient representation of a quantum state does not come for free. By “gluing” the tensors together within the tensor network one gets extra degrees of freedom. These are represented by the connecting indices among the tensors and they are called the *bond indices* of the tensors which have a specific *bond dimension*. These bond indices have an important physical meaning: they describe the entanglement properties of the many-body state and additionally give a quantitative measurement of the amount of quantum correlations within the wave function.

To understand this better let us consider a pure state in the form

$$|\psi_{prod}\rangle = |\varphi_1\rangle \otimes |\varphi_2\rangle \otimes \cdots \otimes |\varphi_N\rangle \quad (3.8)$$

for some $|\varphi_k\rangle$. To represent such a product state with a TN, one would have to represent each subsystem $|\varphi_k\rangle$ with a separate tensor. Since the total wave function is given by a product of such subsystems, the tensors would be trivially connected with a bond dimension $D = 1$. If there is some form of entanglement within the system, the connection between the tensors will be non-trivial which means that a larger bond dimension is needed to give an accurate description of the quantum state.

3.4 AREA-LAW IN TENSOR NETWORK STATES

The bond dimension is the limiting factor in the amount of entanglement the tensor network can encompass and thus there must be an upper bound of entanglement which can be described by a certain bond dimension. To determine this upper limit let us consider a subsystem

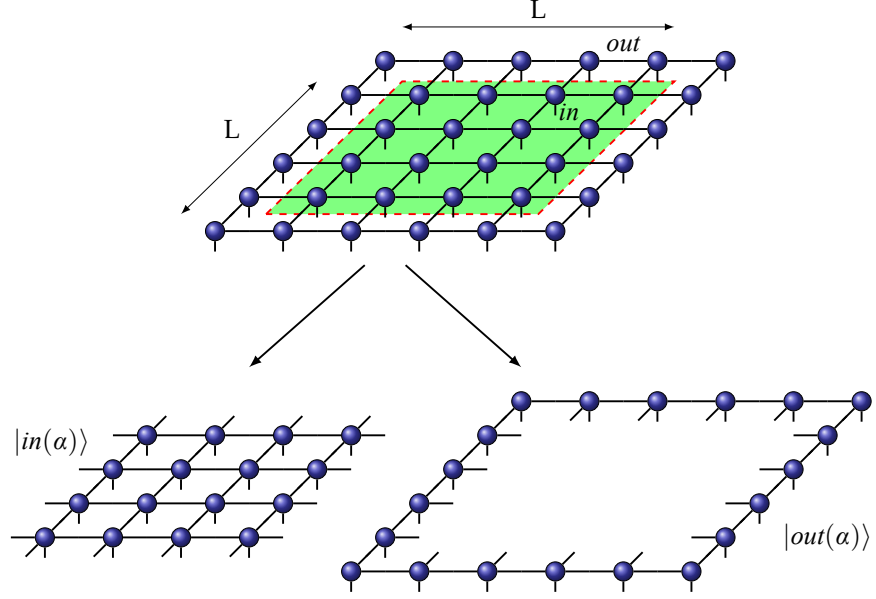


Figure 3.8: Subsystem of a given TN, to calculate the amount of entanglement between the two systems

of a TN² (see fig. 3.8) and calculate the entanglement entropy of this block. Let us assume that all indices of the outer and inner system are combined into one single index $\alpha = \{\alpha_1 \alpha_2 \dots \alpha_{4L}\}$. Thus the total wave function is given by

$$|\Psi\rangle = \sum_{\alpha=1}^{D^{4L}} |in(\alpha)\rangle \otimes |out(\alpha)\rangle \quad (3.9)$$

and the reduced density matrix of the inner part can be written as

$$\rho_{in} = \sum_{\alpha, \alpha'} X_{\alpha\alpha'} |in(\alpha)\rangle \langle in(\alpha')| \quad (3.10)$$

where $X_{\alpha\alpha'} = \langle out(\alpha') | out(\alpha) \rangle$. The maximal rank of the reduced density matrix is clearly given by D^{4L} . If we considered the outer part the result would be the same. The entanglement entropy $S = -\text{tr}(\rho_{in} \log \rho_{in})$ is therefore bounded by the logarithm of the rank of ρ_{in} . This means that

$$S(L) \leq 4L \log(D). \quad (3.11)$$

Equation (3.11) is nothing else than an upper-bound represented by the area law for the entanglement entropy. Another way to look at it is that the amount of “broken” links within the separation in the two systems is $4L$ and each of these “broken” links gives a $\log(D)$ maximum contribution to the total entanglement entropy.

² We will calculate everything for the case of a 2D PEPS, but the concept is still valid in other dimension.

3.5 NUMERICAL TN METHODS FOR INFINITE PEPS

Now that we established the usefulness of TNs, let us explore the numerical methods which can be used to determine the TN state of the ground state for a given Hamiltonian or to calculate expectation values.

All of the following algorithms are only valid for an infinite PEPS lattice which is translationally invariant by construction. It is also possible to consider finite PEPS for small lattices, where each lattice site is described by a different tensor. This however is restricted to rather small lattices.

3.5.1 Finding the ground state

There are different methods to calculate the ground state wave function for a certain Hamiltonian, e.g. *imaginary time evolution* or *variational optimization*. Here we will focus on the *imaginary time evolution* since this method is used in this thesis.

It is known that the ordinary time evolution of a quantum state is given by

$$|\Psi(t)\rangle = e^{-it\mathcal{H}} |\Psi(0)\rangle. \quad (3.12)$$

For the imaginary time evolution we make the transition $t \rightarrow -it$, because for long imaginary times the resulting wave function tends to be the ground state $|E_0\rangle$.

$$\begin{aligned} e^{-\tau\mathcal{H}} &= \sum_j e^{-E_j\tau} |E_j\rangle \langle E_j| = e^{-E_0\tau} \left(\sum_j e^{-(E_j-E_0)\tau} |E_j\rangle \langle E_j| \right) \\ &= e^{-E_0\tau} (|E_0\rangle \langle E_0| + e^{-\Delta\tau} |E_1\rangle \langle E_1| + \dots) \\ &\quad \text{with } \Delta = E_1 - E_0 \end{aligned} \quad (3.13)$$

In the limit of infinite time ($\tau \rightarrow \infty$), this results in

$$e^{-\tau\mathcal{H}} \approx e^{-E_0\tau} |E_0\rangle \langle E_0|. \quad (3.14)$$

Hence

$$|E_0\rangle = \lim_{\tau \rightarrow \infty} \frac{e^{-\tau\mathcal{H}} |\Psi(0)\rangle}{\sqrt{\langle \Psi(\tau) | \Psi(\tau) \rangle}} \quad (3.15)$$

for any initial quantum state $|\Psi(0)\rangle$ which has a non-zero overlap with the ground state.

The basic idea is now to implement such an imaginary time evolution on TN states, e.g. PEPS, for a given Hamiltonian. The first step in such an algorithm is to split the time evolution operator for a certain timestep τ into many operators of very small timesteps so that

$$e^{-\tau\mathcal{H}} = \left(e^{-\delta\tau\mathcal{H}} \right)^m \quad (3.16)$$

where $m = \tau/\delta\tau \gg 1$. For the sake of simplicity let us assume that the Hamiltonian only consists of two-body nearest neighbor terms and it can be written as

$$\mathcal{H} = \sum_{\langle ij \rangle} h_{ij} \quad (3.17)$$

where the sum goes over the nearest neighbors in the lattice. Thus the time evolution operator is given by

$$e^{-\delta\tau\mathcal{H}} = e^{-\delta\tau \sum_{\langle ij \rangle} h_{ij}}. \quad (3.18)$$

Now we do a *first-order Suzuki-Trotter expansion*[54] to decompose the operator into the product of many so-called *two-body gates*

$$e^{-\delta\tau \sum_{\langle ij \rangle} h_{ij}} = \prod_{\langle ij \rangle} e^{-\delta\tau h_{ij}} + \mathcal{O}(\delta\tau^2). \quad (3.19)$$

This also gives us the two-body gate g_{ij} between the sites i and j

$$g_{ij} = e^{-\delta\tau h_{ij}}. \quad (3.20)$$

If we now combine all of the above, we find that the imaginary time evolution can be approximated by letting $U(\delta\tau) = \prod_{\langle ij \rangle} g_{ij}$ act $m \gg 1$ times on a given TN state. This process can be written as a TN diagram and it can be seen for a one-dimensional system in figure 3.9. The extension into two dimensions is straight forward from this.

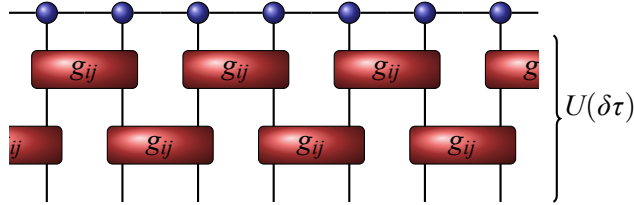


Figure 3.9: Applying the two-body gates m times on the the initial one dimensional TN state. The extension into more dimensions is straight forward.

There are now two steps one has to perform to obtain the ground state in the TN state form:

- (1) **APPLYING $U(\delta\tau)$:** apply $U(\delta\tau)$ to the given TN state $|\Psi\rangle$ with bond dimension D . Afterwards one has a new TN state $|\tilde{\Psi}\rangle = U(\delta\tau) |\Psi\rangle$ with a new bond dimension $\tilde{D} \geq D$
- (2) **TRUNCATE:** find a new state $|\Psi'\rangle$ which approximates $|\tilde{\Psi}\rangle$ but with the reduced bond dimension D

This method of finding the ground state is known as the infinite time-evolving block decimation (iTEBD). There are many ways to perform these two steps which differ in the obtained accuracy and their efficiency. Unfortunately the more accurate methods are less efficient in respect to computational cost whereas more efficient methods tend to be less accurate.

In the following we will explain a method called *simple update*, which is used in this thesis to obtain the ground state for a 2×2 unit cell. Another method called the full update, which is not used in this thesis, is explained in the appendix in section A.1. This method gives more accurate results but requires more computational resources.

Very recently there was a proposal about a new method (the so-called *fast full update*) which would be very accurate but much more efficient as previous algorithms with the same accuracy [48].

3.5.2 Simple Update

Within the simple update the truncation of the larger bond dimension is done via a singular value decomposition in the corresponding link. We start from our PEPS with a 2×2 unit cell and translational invariance as it can be seen in figure 3.10. For the simple update we choose a PEPS with additional tensors λ which carry the information of a specific link in the form of singular values as shown in figure 3.10 (b).

Now we take only two tensors with the connecting λ of the unit cell and apply the two-body gate g_{ij} on the connecting link. Then we combine all four tensors into one large tensor with 8 indices. This large tensor must be separated again to obtain the new updated tensors $\tilde{\Gamma}_A$, $\tilde{\Gamma}_B$ and $\tilde{\lambda}$ for the updated unit cell. Therefore we perform a singular

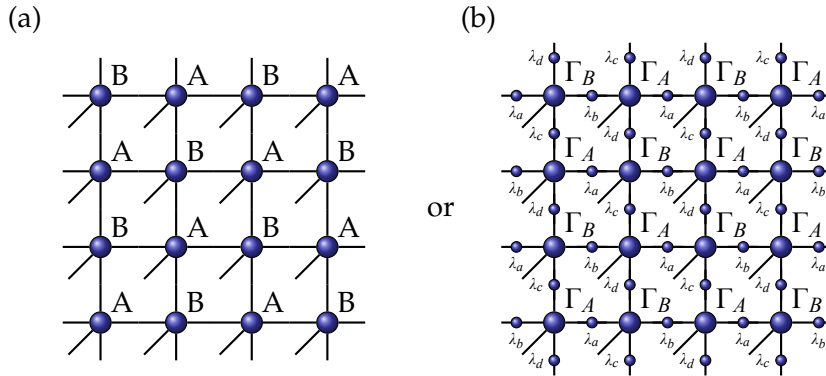


Figure 3.10: PEPS with a 2×2 unit cell and translational invariance. On the left side we see a PEPS which only consists of two tensors A and B. Within the TN on the right side each link has an additional tensor which carries specific information about this link in the form of singular values.

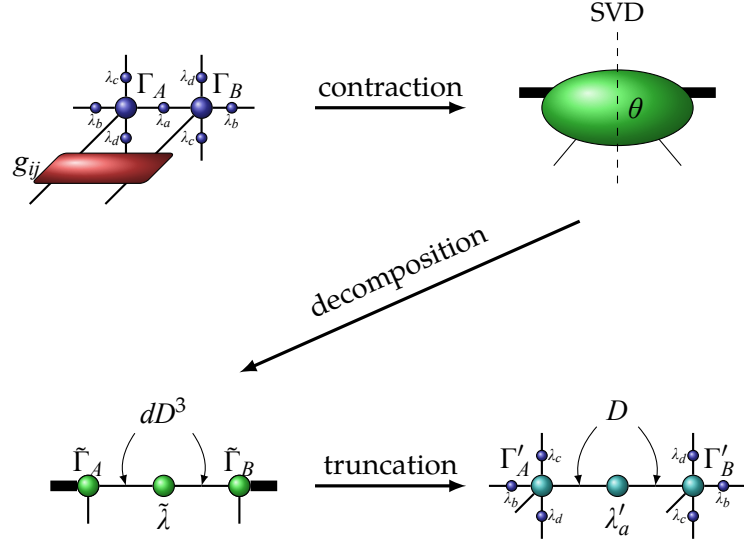


Figure 3.11: TN diagram of the simple update. First one contracts all tensors into one large tensor. Afterwards one has to perform a SVD to decompose this large tensor back into smaller tensors. The last step is to truncate in the largest singular values to ensure that the bond dimension does not grow with each step. The λ 's therefore carry all the singular values corresponding to one specific link. Since all λ 's get absorbed in the first step one has to extract them again in the end from the new Γ 's by multiplying with the corresponding inverse.

value decomposition between the indices corresponding to Γ_A and Γ_B . Afterwards we have again two separate tensors $\tilde{\Gamma}_A$ and $\tilde{\Gamma}_B$ and one intermediate tensor $\tilde{\lambda}$ which carries the singular values.

The bond dimension between $\tilde{\lambda}$ and the two updated tensors is now larger than the original bond dimension between Γ_A and Γ_B and of the order $\mathcal{O}(dD^3)$. This means that we have to truncate this new bond dimension because otherwise the required computational resources would increase after each step.

For this reason, we truncate in the largest singular values of this decomposition. After the truncation we remain with the updated tensors Γ'_A , Γ'_B and λ' . This is the procedure to update one single link of the unit cell, and so we rotate the lattice which now consists of these new tensors, and repeat each step with another link. Since the lattice is translationally invariant we only need to do this for one unit cell and can update every tensor in the lattice afterwards.

This process is repeated iteratively until convergence is reached. The resulting state now approximates the ground state of the given Hamiltonian. The complete process can be seen in the form of TN diagrams in figure 3.11. This approach has only empirical justification since there is no formal reason that it should give near-optimal results. However the empirical results show that this method is very efficient and also gives rather accurate results in some situations. Only close to quantum phase

transitions the method struggles to give good results, because it only takes the short range correlation between two tensors into account. It does not consider the long range parts only visible in the environment of the tensors, which is not taken into account here.

3.5.3 Calculating expectation values

As for finding the ground state for a given Hamiltonian in its TN representation, there are many different methods to calculate the expectation value of some observable for a TN state. For finite systems one could always think of doing the exact contraction of the corresponding tensor network like shown in figure 3.12.

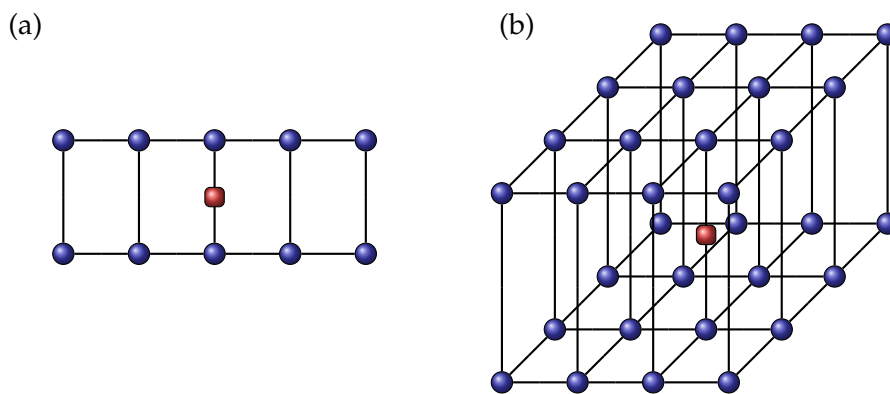


Figure 3.12: Tensor networks for calculating the expectation values for (a) MPS and (b) PEPS

However for an infinite PEPS an exact contraction is not possible and one must find a way to approximate the result.

3.5.3.1 Corner Transfer Matrix

One method is the so called *directional corner transfer matrix (CTM) algorithm* [47]. This method approximates the infinite plane, or more precisely one corner of it, in one single tensor, the so-called corner transfer matrix (see fig 3.13). We will only explain the CTM algorithm for con-

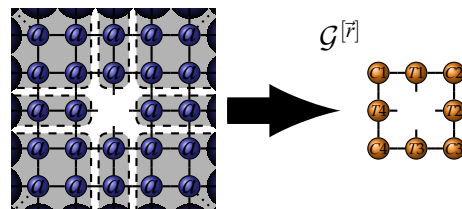


Figure 3.13: Approximating the infinite plane through four corner transfer matrices and two half-row and half-column transfer matrices.

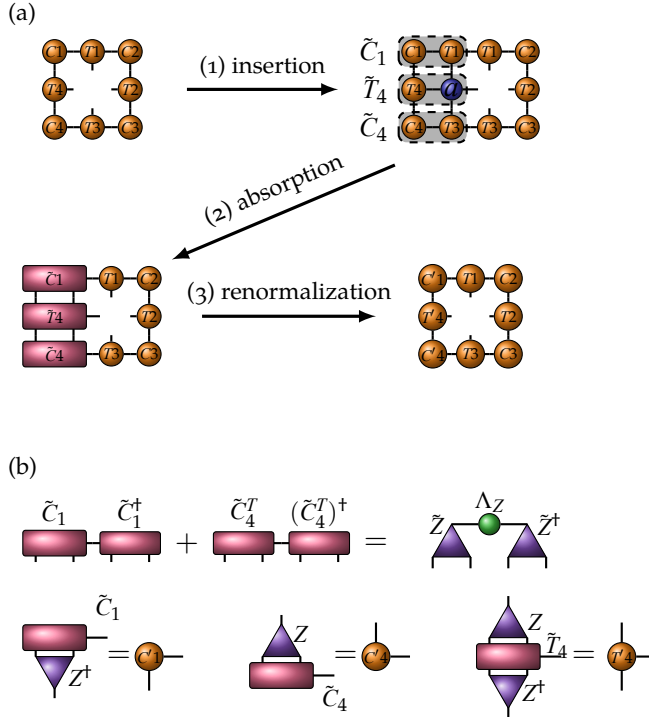


Figure 3.14: Tensor network diagram of the CTM algorithm. In (a) a x-move is shown and (b) shows the renormalization scheme for the updated tensors.

tracting an infinite plane, but the extension to two layers, as it is needed to calculate expectation values for PEPS, is straight forward.

The goal of the CTM algorithm is to find the four fix-point tensors to get an approximate environment $\mathcal{G}^{[r]}$. This environment is given by the simple TN consisting of the tensors $\mathcal{G}^{[r]} = \{C_1, T_1, C_2, T_2, C_3, T_3, C_4, T_4\}$, where C_1, C_2, C_3, C_4 represent the four corner transfer matrices and the two half-column and half-row matrices are given by T_1, T_2, T_3, T_4 . The corresponding TN diagram can be seen in figure 3.13.

To find these tensors one performs iteratively so called *coarse-graining moves* into different directions (up, down, left, right) until the environment converges. For a given environment such a move consists of three main steps which will be explained for a left move. They are also graphically represented in figure 3.14 (a).

- (1) INSERTION: Insert a new column out of the tensors T_1, T_2 and T_3 .
- (2) ABSORPTION: Absorb this new column into the already existing left border to obtain the new \tilde{C}_1, \tilde{T}_4 and \tilde{C}_4 .
- (3) RENORMALIZATION: Due to the fact that the dimension of the new tensor is now larger than before one must renormalize with some isometry Z ($Z^\dagger Z = \mathbb{1}$).

The choice of the isometry Z is very important to get accurate results, but there is no canonical choice which yields the best result. One possi-

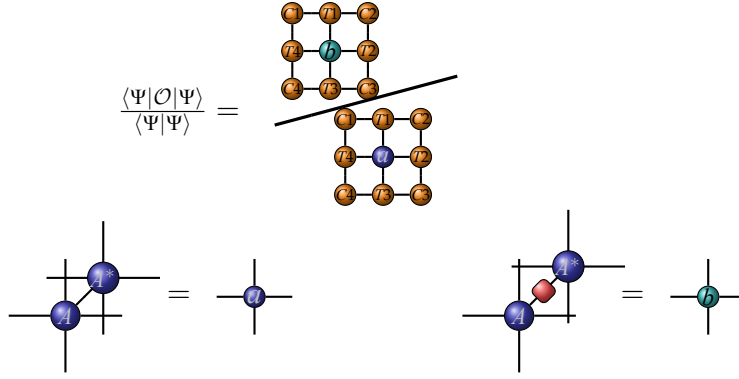


Figure 3.15: Expectation value of some one-site observable

bility is to use the eigenvalue decomposition of the product of the four CTM's $\tilde{C}_1 C_2 C_3 \tilde{C}_4$. However, here we consider the eigenvalue decomposition of $\tilde{C}_1 \tilde{C}_1^\dagger + \tilde{C}_4 \tilde{C}_4^\dagger = \tilde{Z} \Lambda_Z \tilde{Z}^\dagger$ instead as shown in figure 3.14 (b). The isometry Z results from \tilde{Z} by keeping the entries which correspond to the D largest eigenvalues of Λ_Z . Now one iterates the four moves until the environment converges.

From this environment it is very easy to calculate expectation values. The only thing that is left to do is to insert a tensor in the middle and do a final contraction of the complete TN.

The tensor which is usually put in the middle of the environment is the contraction of the PEPS-tensor with some operator. Since our TN states are in general not normalized one must also compute the norm of the state with the same method. The resulting expectation value is then given by the ratio of two tensor networks which differ only in one single tensor (figure 3.15). All of the explained steps above are only valid for a unit cell of size one. However we use a larger 2x2 unit cell within this thesis. The extension to a larger unit cell is straight forward from the algorithm explained above and is described in more detail within the appendix in section A.2.

3.5.3.2 Higher Order Tensor Renormalization Group Algorithm ³

Another way to calculate the expectation value for some observable is to do a *coarse-graining* of the tensor network. For this coarse-graining we contract the TN alternately along the horizontal (x-axis) and vertical (y-axis) directions. This means that for each step we contract two adjoining tensors along one axis into one single tensors M which represents one site in the coarse-grained lattice. Since the bond dimension of the coarse-grained TN would increase after each iteration we must truncate M into a lower rank tensor. This is done via truncation with

³ This method was proposed in [61]

a *higher order singular value decomposition (HOSVD)*[32]. The resulting decomposition yields

$$M_{xx'yy'} = \sum_{ijkl} S_{ijkl} U_{xi}^L U_{x'j}^R U_{yk}^U U_{y'l}^D \quad (3.21)$$

where each U is a unitary matrix. S is the so called core tensor of M with the following properties

(1) ORTHOGONALITY

$$\langle S_{:j,:,:} | S_{:j',:,:} \rangle = 0 \quad \text{if } j \neq j' \quad (3.22)$$

(2) PSEUDO-DIAGONALITY

$$|S_{:j,:,:}| \geq |S_{:j',:,:}| \quad \text{if } j < j' \quad (3.23)$$

where $|S_{:j,:,:}|$ is the norm of this sub-tensor which is defined as the square root of the sum over all squared elements. These norms have a similar role as the singular values of a matrix. If we do a vertical move, the two vertical indices do not change and do not need to be truncated. Since the right leg of M is connected the left leg of an identical tensor on the right neighbouring side, truncating one of the horizontal links automatically truncates the other one as well. Now we must choose the best way to truncate the horizontal bonds. Since these bonds are linked we can truncate via U^R or U^L . Therefore we compare the norm of the first and second index for all index values above D and we define

$$\varepsilon_1 = \sum_{i>D} |S_{i,:,:}|^2 \quad (3.24)$$

and

$$\varepsilon_2 = \sum_{j>D} |S_{:,j,:}|^2. \quad (3.25)$$

By comparing ε_1 and ε_2 we can decide with which of the two corresponding unitary matrices we must truncate to minimize the error. If $\varepsilon_1 < \varepsilon_2$, we truncate the first dimension of S or the second dimension of U^L to D . In the other case we truncate the second dimension of S or the second dimension of U^R to D . This truncation scheme provides a minimization of the truncation error.

After this step we update the local tensor via

$$M' = \sum_{ij} \tilde{U}_{ix} M_{ijyy'} \tilde{U}_{jx'} \quad (3.26)$$

where $\tilde{U} = U^L$ (or U^R) if ε_1 is smaller (or larger) than ε_2 . We repeat this process now with alternating x- and y-moves until we find a fix-point of the tensor network. This means that in the end we only have one tensor left which describes the complete TN. The expectation value of the

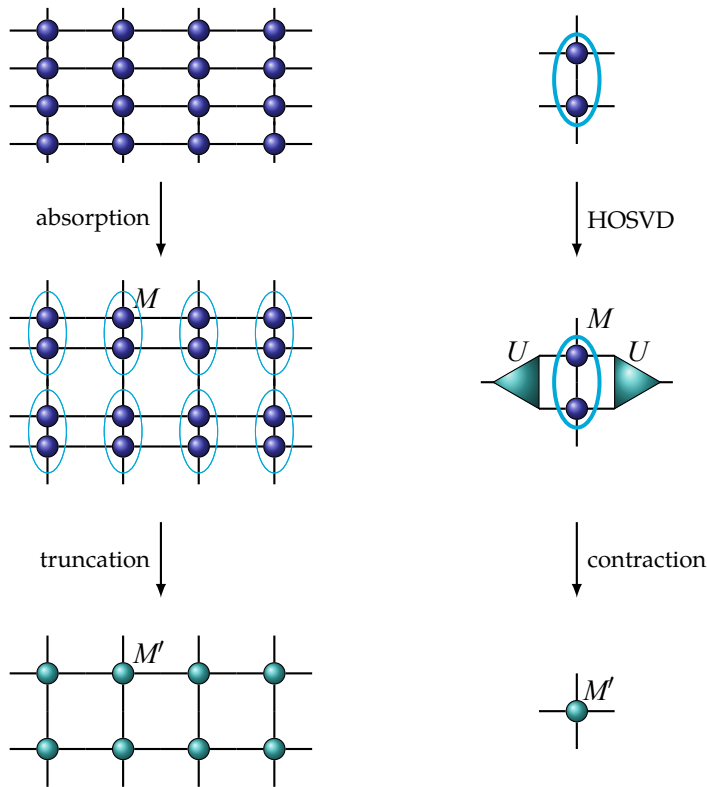


Figure 3.16: On the left side we see a vertical coarse graining move within the HOTRG algorithm and the corresponding truncation scheme can be seen on the right.

tensor network is then given by the contraction of a single tensor. Of course one has to start with a tensor with some observable absorbed to determine its expectation value and additionally calculate the corresponding norm.

The algorithm explained above does not work for a double layered lattice without further extensions. This means that in our case we must first combine the bra and ket PEPS into one single tensor. This has the disadvantage that the resulting bond dimension in this tensor network is the dimension of the original PEPS squared. As a consequence of this squaring, one can only use this method for rather small bond dimensions (see sec. 3.5.4).

3.5.4 Computational Complexity

All the methods for calculating expectation values and ground states have different computational complexity.

The computational cost of the tensor contractions and multiplications is given by the number of computational cycles which are needed to perform the operation. For the computational cost of a complete algorithm we only keep track of the step with the highest cost.

In general the computational cost of a simple matrix multiplication between two matrices $A_{\alpha\beta}$ and $B_{\beta\gamma}$ is of the order $\chi_\alpha\chi_\beta\chi_\gamma$ where χ_i is the size of the corresponding dimension.

The memory requirement for such an operation is given by $\chi_\alpha\chi_\beta + \chi_\beta\chi_\gamma + \chi_\alpha\chi_\gamma$. For the contraction of a complete tensor network with many tensors the computational cost and the memory requirement are strongly dependent on the contraction order of the network. Usually one tries to minimize the time needed for finding ground states or expectation values by choosing the order of contraction with the lowest computational cost. On the other hand one has to keep track of the needed memory, since the contraction which optimizes the computational cost is not necessarily the most efficient one concerning the memory requirement.

By following the rules for determining the computational cost and memory usage we obtain the following values for the algorithms explained above.

ALGORITHM	COMPUTATIONAL COST	MEMORY REQUIREMENT
Simple Update	$\mathcal{O}(d^4q^2D + (dq)^3)$	$\mathcal{O}(d^4qD)$
CTM	$\mathcal{O}(\chi^2d^2D^7)$	$\mathcal{O}(\chi^2d^2D^4)$
HOTRG	$\mathcal{O}(D^{14})$ and $\mathcal{O}(\chi^7)$	$\mathcal{O}(D^{12})$ and $\mathcal{O}(\chi^6)$

Table 3.1: The computational cost and memory requirement for the different algorithms. d is the physical dimension, D the bond dimension of the PEPS, $q \equiv \min(D^3, dD)$ and χ the bond dimension of the environment. In the case of the HOTRG algorithm the computational cost scales with $\mathcal{O}(D^{14})$ in the very first step before the truncation and with $\mathcal{O}(\chi^7)$ afterwards.

By comparing the different scalings of our methods one can easily see that the HOTRG algorithm scales very badly in computational time and memory usage. Therefore this algorithm can only be used for bond dimensions smaller than six. For bond dimensions of six and larger the memory usage exceeds the maximum amount of RAM which was available during this thesis.

However, the HOTRG algorithm does not scale with the physical dimension of the model. Therefore it can be used to determine the expectation values of systems with very large physical dimensions.

Part II

BENCHMARKING OF THE CODE

THE 2D CLASSICAL ISING MODEL

4.1 THE MODEL

The Ising model is one of the best-studied models in statistical physics. It is used to describe ferromagnetism in solids by assuming that the spins in the solid belong to a two level system and only neighbouring sites interact with each other.

This interaction between two sites can be either ferromagnetic or anti-ferromagnetic in nature. This depends, of course, on the system one is looking at. In the further discussion in this thesis we will restrict ourselves to the ferromagnetic case, where the parallel pairing of spins is favoured.

In the classical case, we will look at this model for finite temperatures and look for phase transitions. That a phase transition must occur can easily be seen by looking at the cases of very large temperature and vanishing temperature. At $T = 0$ the solution of this system becomes trivial since it spontaneously breaks the \mathbb{Z}_2 -symmetry of the up and down spins and the system lies in a state in which all spins are aligned either up or down. This means that we find a completely ordered state at $T = 0$. For infinite temperature on the other hand the thermal fluctuations become so large that we have a completely disordered state which restores the inherent \mathbb{Z}_2 -symmetry.

Since we have a completely ordered state on one side and a disordered state on the other side there must be some sort of phase transition in between. For the square lattice the model has been solved by Onsager [45] and this phase transition point has been determined.

The fact that we have a phase transition at a finite temperature is rather rare within two dimensions, since the Mermin-Wagner-Theorem [37] states that continuous symmetries cannot be spontaneously broken at finite temperatures for one and two dimensional systems. This means that one will not find phase transitions at finite temperatures for systems with continuous symmetries. The Ising model however has a discrete symmetry which allows for such a phase transition.

4.2 RESULTS

In this section we will discuss how the algorithms explained in chapter 3 can be used to calculate the expectation values and correlation functions for this classical system. Here we will consider the classical

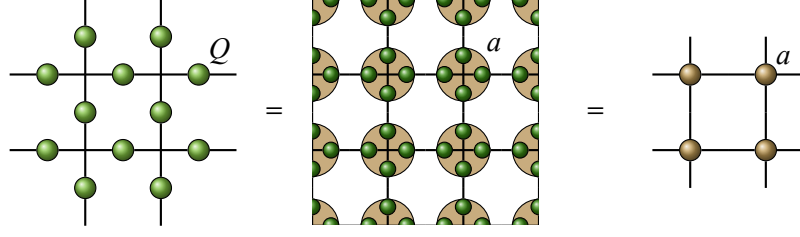


Figure 4.1: The partition function of the 2D classical Ising model can be as the contraction of a 2D tensor network which only consists of one tensor a on each site

Ising model on the infinite 2D square lattice. The interaction between two neighbouring sites $\langle \vec{r}, \vec{r}' \rangle$ in this model is given by

$$K_2(s, s') = -ss' \quad (4.1)$$

and therefore the Hamiltonian K is given by

$$K(\{s\}) = \sum_{\langle \vec{r}, \vec{r}' \rangle} -s^{[\vec{r}]}s^{[\vec{r}']}. \quad (4.2)$$

The corresponding partition function is then given by

$$Z(\beta) = \sum_{\{s\}} e^{-\beta K(\{s\})} = \sum_{\{s\}} \prod_{\langle \vec{r}, \vec{r}' \rangle} e^{-\beta K_2(s^{[\vec{r}]}, s^{[\vec{r}']})} \quad (4.3)$$

where β is the inverse temperature. If we define $Q_{ss'} = \exp(-\beta K_2(s, s'))$, we can express the partition function as the contraction of an infinite 2D tensor network specified by a single tensor a

$$a_{ijkl} = \sum_s (\sqrt{Q})_{is} (\sqrt{Q})_{js} (\sqrt{Q})_{ks} (\sqrt{Q})_{ls} \quad (4.4)$$

on every site, see fig. 4.1. From this partition function we can also calculate expectation values or correlation functions. The expectation value for any function $f(s)$ of one spin is given by

$$\langle f(s^{[\vec{r}]}) \rangle = \frac{1}{Z(\beta)} \sum_{\{s\}} f(s^{\vec{r}}) e^{-\beta K(\{s\})}. \quad (4.5)$$

Up to the prefactor of $1/Z(\beta)$ this can also be written as the contraction of an infinite 2D TN which is very similar to the TN of $Z(\beta)$. The only difference is that one has to replace the tensor a on site \vec{r} with b ,

$$b_{ijkl} = \sum_s f(s) (\sqrt{Q})_{is} (\sqrt{Q})_{js} (\sqrt{Q})_{ks} (\sqrt{Q})_{ls}. \quad (4.6)$$

Thus the expectation value is given by the ratio of the total contraction of two tensor networks which only differ in one tensor. This is shown in figure 4.2.

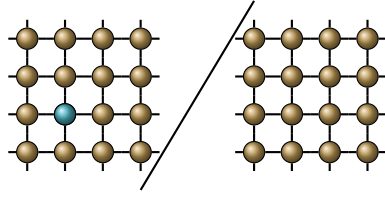


Figure 4.2: The expectation value is given by the ratio of two tensor networks which only differ in the tensor on site \vec{r}

Since the only difference between these two tensor networks is just one single tensor, we can calculate the environment using the CTM algorithm and use it for both contractions since only the tensor in the middle of the environment changes.

Using this one can calculate the magnetization per site $m \equiv \langle s^{\vec{r}} \rangle$ and compare it to the exact solution[45] which is given by

$$m = \left(1 - \sinh(2\beta)^{-4}\right)^{\frac{1}{8}} \quad (4.7)$$

The numerical values which were obtained by the CTM algorithm are shown in figure 4.3. One can clearly see that the agreement of the numerical results and the analytical results is very good. Even near the phase transition, which occurs at the critical inverse temperature

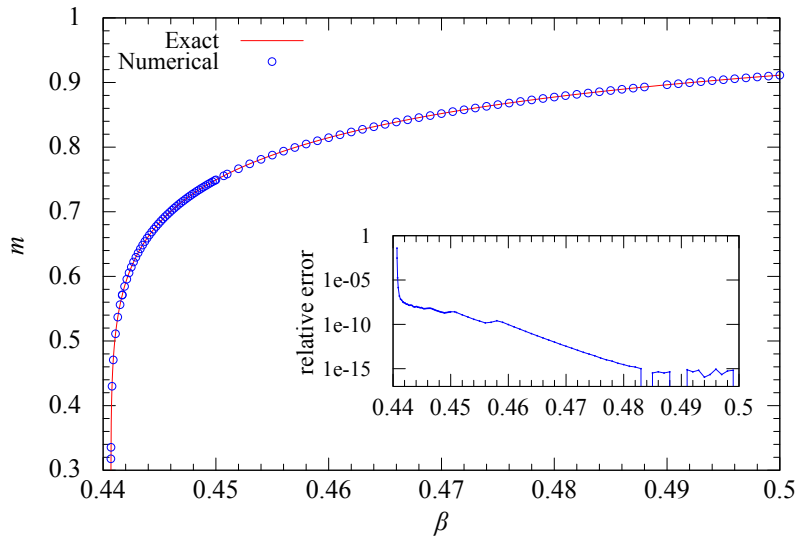


Figure 4.3: Magnetization per lattice site for the 2D classical Ising model on the infinite lattice plotted against the inverse temperature β . The exact solution is also shown as well as a plot of the relative error between the calculation and the exact solution. The bond dimension of the environment in this calculation is $\chi = 40$.

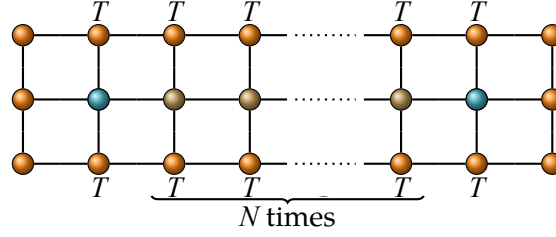


Figure 4.4: Calculating the correlator between two sites by inserting N half-column transfer matrices

$\beta_c = 1/2 \log(1 + \sqrt{2})$, the relative error is only around 1%. Away from the criticality the error decreases to $\approx 10^{-15}$, which means that our numerical calculation is in very good agreement with the analytical results.

In addition to single site expectation values one also can calculate the expectation value of e.g. the correlator

$$\langle f(s^{\vec{r}})g(s^{\vec{r}'}) \rangle = \frac{1}{Z(\beta)} \sum_{\{s\}} f(s^{\vec{r}})g(s^{\vec{r}'})e^{-\beta K(\{s\})}. \quad (4.8)$$

Similar to the single site expectation value we can write it as a TN very similar to $Z(\beta)$, except for two tensors on the sites \vec{r} and \vec{r}' which are replaced by the corresponding tensors b and b' . In this case we must extend the environment to contract the tensor network by inserting N more half-column transfer matrices and tensors a where N is the number of sites in between \vec{r} and \vec{r}' (see fig. 4.4). The decay of the spin-spin correlator $\langle s^{\vec{r}}s^{\vec{r}'} \rangle$ with the distance $|\vec{r} - \vec{r}'|$ at the critical point $\beta_c = 1/2 \log(1 + \sqrt{2})$ can be seen in figure 4.5.

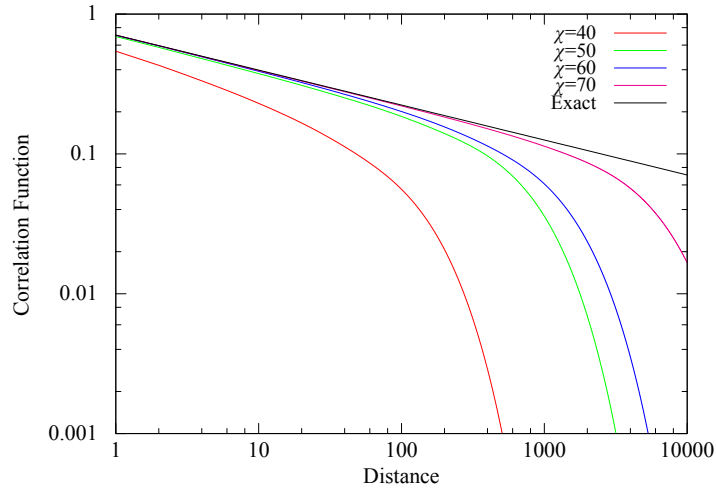


Figure 4.5: The two point spin-spin correlator for the 2D quantum Ising model. With the increase of the bond dimension of the environment the correlation function converges against an algebraic decay. For a bond dimension of $\chi = 70$ the algebraic decay can be reproduced up to a distance of about 1000 spins.

The accuracy of the numerical results increases with the bond dimension of the calculated environment and the power-law decay can be reproduced for distances up to 1000 spins.

Now we have shown that with our CTM algorithm we are able to calculate the expectation value of a two dimensional lattice system with high accuracy. The relative error of our calculation is only around $\sim 10^{-2}$ at the critical point and decays down to $\sim 10^{-15}$ away from criticality.

Additionally, we are able to calculate two-point correlation functions with good agreement with the analytic results up to a distance of 1000 spins. For the algebraic decay of the correlation function a higher bond dimension ($\chi = 70$) is needed than for accurate expectation values ($\chi = 40$). This is due to the fact that for larger long-range correlations also higher bond dimensions are needed. But, since $\chi = 70$ is still very well accessible, one can conclude that the corner transfer matrix algorithm is a very good tool to calculate expectation values and correlation functions for two dimensional lattice systems.

THE 2D QUANTUM ISING MODEL

Now that we have seen that the CTM algorithm works well for classical lattice systems we will calculate the properties of a quantum lattice system, strictly speaking the 2D quantum Ising model. In this case we additionally have to approximate the ground state itself via the simple update. From this approximated ground state we will then determine several expectation values with the corner transfer matrix algorithm as well as the HOTRG algorithm. In the end we will compare the obtained results from both methods.

5.1 THE MODEL

The quantum Ising model is a simple and well studied example of interacting spins on a lattice. The corresponding Hamiltonian is given by

$$\mathcal{H} = - \sum_{\langle ij \rangle} \sigma_z^i \sigma_z^j - h \sum_i \sigma_x^i \quad (5.1)$$

where σ_z and σ_x are Pauli operators and h the strength of a external transverse magnetic field. The eigenstates of σ_z are given by $|\uparrow\rangle_z$ and $|\downarrow\rangle_z$ and the eigenstates of σ_x are given by $|\uparrow\rangle_x$ and $|\downarrow\rangle_x$.

If $h = 0$, the ground state is given by a product state of either $|\uparrow\rangle_z$ or $|\downarrow\rangle_z$. Since the Hamiltonian has a \mathbb{Z}_2 -symmetry, which means that it is invariant under $\sigma_z \rightarrow -\sigma_z$, the energy is invariant under $|\uparrow\rangle_z \rightarrow |\downarrow\rangle_z$ and therefore the symmetric ground state $|\Psi_{sym}\rangle$ should have a zero magnetization in the z-direction.

$$\begin{aligned} m_z &= \langle \Psi_{sym} | \sigma_z | \Psi_{sym} \rangle = \langle \Psi_{sym} | -\sigma_z | \Psi_{sym} \rangle \\ &= - \langle \Psi_{sym} | \sigma_z | \Psi_{sym} \rangle \\ &= 0 \end{aligned} \quad (5.2)$$

This symmetric state however is highly unstable in the sense that every small perturbation sets the system off so that it flows into one of the two states and the symmetry is spontaneously broken.

In the limit of very large h , this \mathbb{Z}_2 -symmetry is restored since the ground state is then given by the eigenstates of σ_x and the magnetization $m_z = 0$. Therefore we can use m_z to distinguish between a state which has a broken symmetry and one that still has this \mathbb{Z}_2 -symmetry and thus we call it an *order parameter* of the system.

In the Landau theory of phase transitions, the phases of a system can be distinguished by checking whether the symmetry is conserved or broken. This means that by calculating $m_z(h)$ we can provide the phase diagram and also the phase transition point for this model.

For the two dimensional case, with which we are concerned here, there is no exact solution, but still it is a very well studied model by various numerical techniques, with quantum Monte Carlo (QMC) [5], series expansion (SE)[27] and exact diagonalization (ED) among them. The results from QMC calculations are considered to be the most accurate since it does not suffer from the sign problem for this model. These simulations estimate the phase transition point to be at $h_c \approx 3.044$. It is also strongly suggested that the phase transition is of second order (as in the one dimensional Ising model) with a critical exponent of $\beta \approx 0.327$ [5].

In the following section we will compare our algorithms to these results to give a certain benchmark and justify that these algorithms can be used to study the properties of 2D quantum systems.

5.2 RESULTS

We now want to determine the phase diagram of the 2D quantum Ising model with the help of our tensor network methods. Therefore we calculate the TN ground state of this model for different values of the external magnetic field h .

Afterwards we calculate the expectation values for the energy, the transverse magnetization and the longitudinal magnetization with the CTM-algorithm and the HOTRG-algorithm.

The expectation values of the magnetization in the transverse and longitudinal direction, as well as the energy can be seen in figure 5.1. If we have a closer look at the critical point for different bond dimensions (fig. 5.2), it seems like there is a first-order phase transition at a critical field $h \approx 3.24$. This result is unexpected, since it is well established that

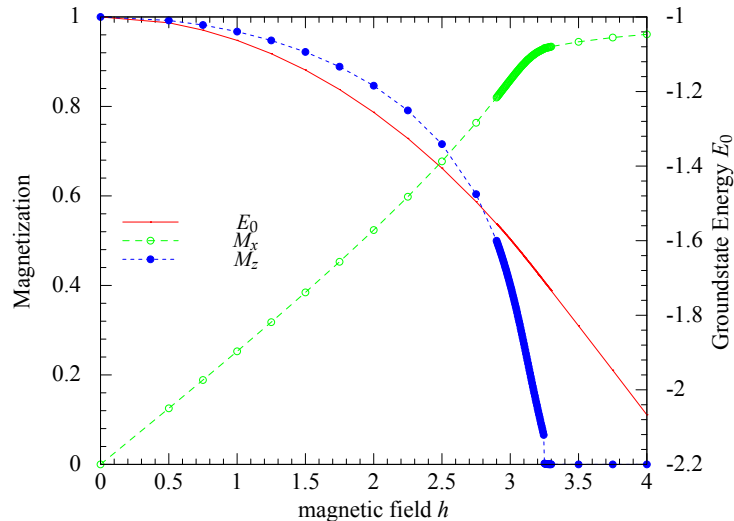


Figure 5.1: The magnetization m_x and m_z and the ground state energy E_0 of the quantum Ising model plotted against the magnetic field.

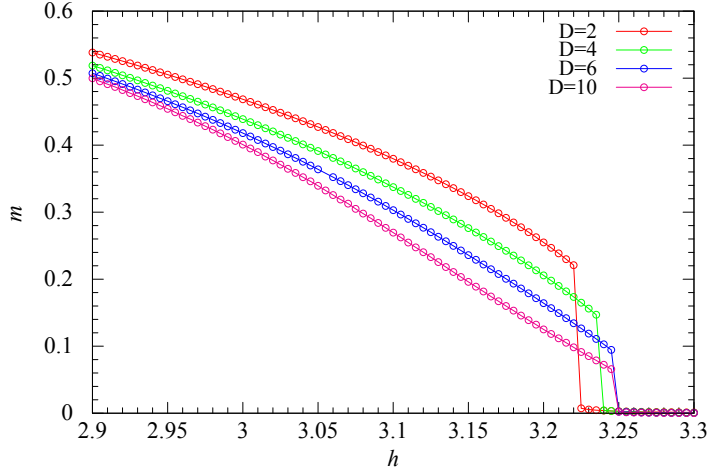


Figure 5.2: Magnetization close to the critical field for several bond dimensions. The jump indicates a first order phase transition.

the 2D quantum Ising model has a second order phase transition at a critical field $h_c \approx 3.044$ (QMC).

However if one looks closely at figure 5.2, one see that the jump decreases with increasing bond dimension. Therefore it seems like our method is not able to encompass the large amount of entanglement at this critical point with the bond dimensions we can access.

Since we are only using the simple update it is also possible that we cannot get a second-order phase transition. The reason for this is that we do not regard the influence of the environment in our algorithm and therefore cannot get any sort of long-ranged entanglement. This, however, is needed at the critical point since the correlation length diverges.

If we now have a look at the magnitude of this jump depending on the bond dimension (fig. 5.3a), it seems like this jump does not vanish completely. However, if we plot it against $1/D$ (see fig. 5.3b) it seems well possible that the jump vanishes at infinite bond dimension if the decay does not follow an exponential function. We therefore cannot conclude with certainty if a certain jump will remain at infinite bond dimension. It is however quite possible that the simple update is not able to encompass the correct behaviour of second order phase transitions, due to the reasons listed before.

Up to now we only used the CTM algorithm to calculate expectation values, but as described in section 3.5.3.2 we have a second algorithm to calculate expectation values. We will now compare these two algorithms. We therefore calculate the magnetization again for a bond dimension of $D = 3$ and $\chi = 10$ with our HOTRG and CTM algorithm and plot both results in figure 5.4. We can see that the general difference between these two methods is rather small.

However it seems like the HOTRG algorithm gives slightly better results for the magnetization, especially shortly before the critical point.

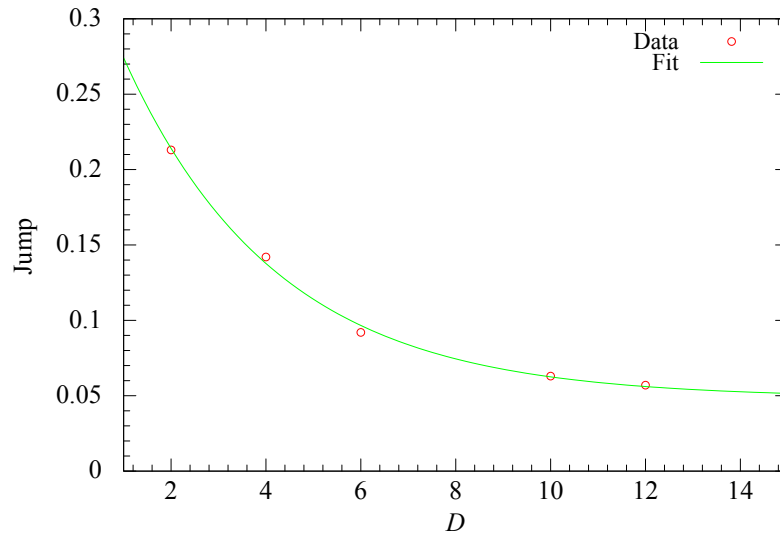
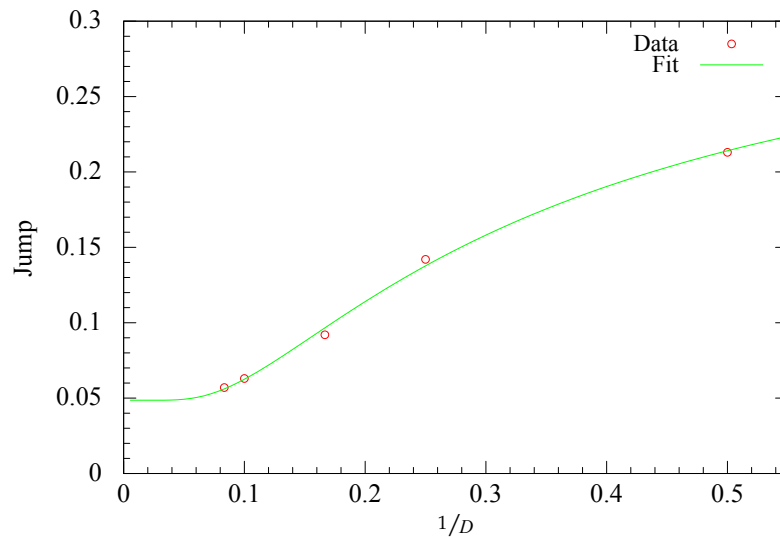
(a) Jump depending on D (b) Jump depending on $1/D$

Figure 5.3: Magnitude of the jump in the apparent first order phase transition of the 2D quantum Ising model depending of the bond dimension of the PEPS. From the exponential fit we can conclude that the jump within the magnetization does not vanish even at very large bond dimensions. In (a) we plotted the jump directly against the bond dimension, whereas in (b) we plotted against $1/D$. From the behaviour of the jump when plotted against $1/D$ it is not clear if the jump will vanish for large bond dimensions or if a finite jump will remain.

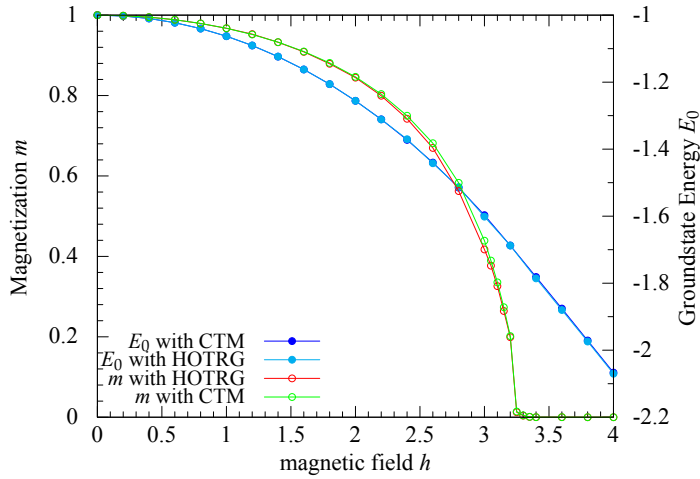


Figure 5.4: Comparison of the CTM and the HOTRG algorithm. The difference between these two algorithms is very small but at some points the HOTRG algorithm seems slightly better. All of the results above are with $D = 3$ and $\chi = 10$.

To examine this deviation between the methods more closely we plot the difference on the expectation values obtained by the CTM and the HOTRG algorithm (see fig. 5.5). If we look at the difference of the magnetization values we can see that the maximum is at a magnetic field of $h = 3$. For very small values of the magnetic field, or for values above the critical value the difference vanishes.

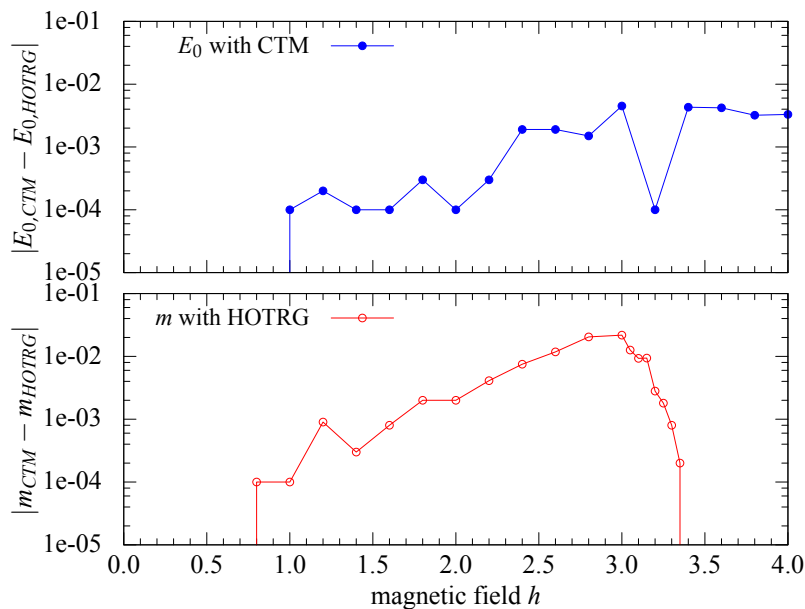


Figure 5.5: The difference between the expectation values obtained by the CTM and HOTRG algorithm

For the difference of the ground state energies, the general picture is very similar except that the difference does not seem to vanish again after the critical point.

From this we could conclude that the HOTRG algorithm gives better expectation values and would be a better method to use. Unfortunately, the HOTRG algorithm scales worse than the CTM algorithm in terms of CPU and memory usage which restricts its usage to rather small bond dimensions. Thus, we are mostly using the CTM algorithm to calculate expectation values further on. We only use the HOTRG algorithm in some cases where we have extremely large physical dimensions, since the CPU and memory usage does not scale with this dimension.

Part III

THE HEISENBERG MODEL ON THE KAGOME
LATTICE

INTRODUCTION

Up to now every model we looked at was living on the square lattice. However, in solid state physics not every system has this specific kind of geometry. Many lattice systems, like crystals, have quite different geometries (e.g. a triangular or honeycomb lattice structure). This change of the underlying structure can give rise to a lot of interesting physics and new states of matter.

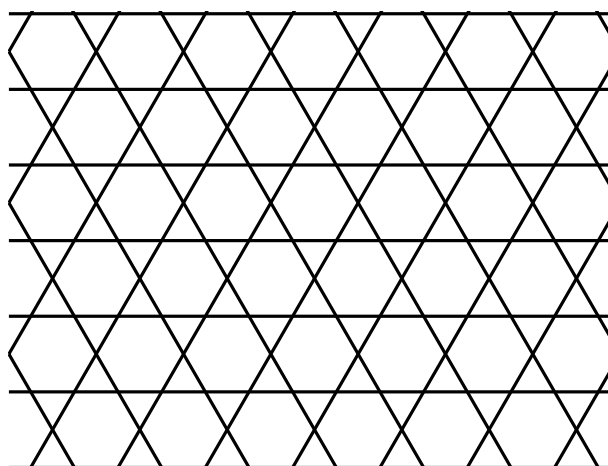


Figure 6.1: The lattice structure of the kagome lattice. It is a lattice which consist of hexagons and triangles. It can also be seen as a triangular lattice out of triangles by looking at e.g. the up-triangles.

One very interesting lattice is the so-called *kagome* lattice (figure 6.1) because it gives rise to large amounts of geometric frustration which yield very strong quantum fluctuations. In physics, frustration refers to the presence of competing forces that cannot be simultaneously satisfied. One very simple example for this effect is an antiferromagnetic model, in which all neighboring spins want to anti-align, on a triangular lattice. In this case, it is not possible that all three spins within a triangle anti-align at the same time. There will always be a site in which it is not clear what value the spin will take (either up or down)(see figure 6.2). The kagome lattice has even larger amounts of geometric frustration than the triangular lattice, because it can be seen as a triangular lattice with again triangles on each lattice site.

These large amounts of frustration make this model very interesting since it is anticipated to give rise to new quantum states of matter, like quantum spin liquids[1] or simplex solids[28].

The name kagome comes from the two Japanese words *kago* which means basket and *me* meaning eyes. It refers to the pattern of a traditional Japanese woven bamboo basket (fig 6.3). The model which

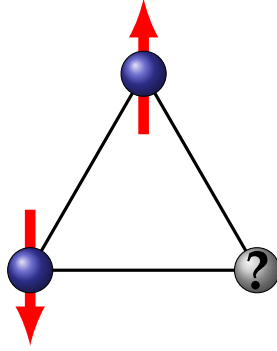


Figure 6.2: Graphical representation of the frustration within a triangular lattice

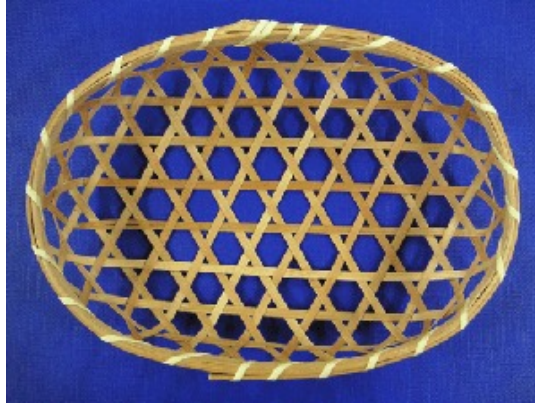


Figure 6.3: Japanese Basket showing the typical woven pattern which is known as the kagome lattice[41].

we want to study now on the kagome lattice is the antiferromagnetic Heisenberg model, the basic model to describe the spin interaction within antiferromagnets. The corresponding hamiltonian is given by

$$\mathcal{H} = - \sum_{\langle ij \rangle} \vec{S}_i \vec{S}_j. \quad (6.1)$$

This model describes the interaction between neighboring spins on a lattice and can be seen as the strong-coupling limit of the Hubbard model of electrons. It has full $SU(2)$ -symmetry and is used to describe simple forms of magnetism, like anti- or ferromagnetism, on a fundamental level.

We will now investigate this model on the kagome lattice for different spins, i.e. the spin- $1/2$, 1 and $3/2$ case.

THE SPIN- $1/2$ KAGOME HEISENBERG ANTIFERROMAGNET

In this chapter we are looking at the spin- $1/2$ case for the Heisenberg model on the kagome lattice. This model has been subject to a lot of discussion, since the nature of its ground state is still controversial after more than 20 years of research on this topic [14, 17, 21, 26, 30, 36, 50, 53, 58, 60, 62, 63]. The reason for this is that this model suffers from the large amount of frustration of the underlying lattice. This makes it very hard to tackle this problem analytically as well as numerically.

Thus many different methods were applied to this model, to get a better understanding of the underlying physics. This variety of methods include MERA [17], coupled cluster methods [21], DMRG [62] and many more. Monte Carlo methods are not able to tackle this problem due to the sign problem [39] which restricts its usage from frustrated systems. In this section we are using our PEPS approach and try to determine the properties of the corresponding ground state.

One proposed ground state was the so called quantum spin liquid (QSL), proposed by Anderson [1]. This is a very unusual state as far as ground states are concerned. The reason for this is that ground states usually break some symmetries of the corresponding Hamiltonian, like the \mathbb{Z}_2 symmetry in the Ising case or gauge symmetry in superconductors. The quantum spin liquid on the other hand does not break any symmetry of the parent Hamiltonian. The name comes from the analogies to a classical liquid, in which the molecules form a dense and highly correlated state which has no static order. Although we all know this kind of phase from our every day life and it is very common in the classical world, a spin liquid is a very exotic phase of matter and has only been seen in very few materials [23]. It is also hard to find numerically in realistic models.

Another ground state that was proposed is some sort of *valence bond crystal* (VBC). In such a state two spins form a spin-0 singlet due to the antiferromagnetic interaction. These two spins form then a so called *valence bond*. The ground state then would consist of some ordering in which every spin in the lattice is bound in such a singlet. The two spins within such a valence bond are maximally entangled, but not entangled with any other spin of the system. Such a VBC however is quite different from a QSL, since it usually breaks a lattice symmetry by choosing one specific arrangement of these valence bonds. Additionally it also lacks the long-range entanglement and topological order which may be present within a QSL[1].

Even though there is a clear difference between a VBC and a QSL it is possible to construct a QSL from a VBC. A VBC usually breaks lattice symmetries, since the arrangement of the bonds on the lattice is not unique, and lacks long-ranged entanglement. If the valence bonds are allowed to undergo quantum-mechanical fluctuations, the quantum state will be a superposition of different partitionings of spins into valence bonds. If the distribution of partitionings is broad, and no specific order is preferred, the state can be regarded as a valence bond liquid, rather than a valence bond solid or crystal. Such a state, which is based on many different VBCs, is called a *resonating valence bond state* (RVB) which was first proposed by Anderson[1]. One way to obtain such an exotic state of matter is through very strong quantum fluctuations which prohibit the system from choosing one specific valence bond order, but favour a superposition of all orderings.

Which of these proposed ground states is the true one for the spin-1/2 Heisenberg model on the kagome lattice is not yet completely clear. Some numerical studies favour a VBC and some tend towards a QSL, but the lowest results which are obtained so far seem to favour a \mathbb{Z}_2 -QSL over the VBC[14].

The kagome lattice with spin-1/2 Heisenberg-like interaction also appears in nature within some mineral compounds, e.g. in the minerals *herbersmithite* ($\text{ZnCu}_3(\text{OH})_6\text{Cl}_2$), *volborthite* ($\text{Cu}_3\text{V}_2\text{O}_7(\text{OH})_2 \cdot 2\text{H}_2\text{O}$) or *vesignieite* ($\text{BaCu}_3(\text{OH})_6\text{Cl}_2$). The ground states of these materials are now subject to a lot of studies to determine if it is a QSL or a VBC. At the moment the experimental results seem to favour a \mathbb{Z}_2 -QSL as the ground state of these materials[23].

7.1 MAPPING TO THE SQUARE LATTICE

The PEPS-algorithms explained in chapter 3.5 are only valid on a square lattice. This means that we either have to modify the algorithms to be valid on this special lattice or perform a mapping between the kagome and the square lattice.

Modifying the algorithms for the kagome lattice has proven to be quite difficult and we therefore try to map it onto the square lattice.

This mapping is done via combining three lattice sites from the kagome lattice into a single site of the square lattice. We therefore combine the two sites from the bottom of each hexagon in the kagome lattice with the leftmost site of the hexagon (see fig. 7.1). After this mapping each link in the square lattice corresponds to two links in the kagome and the physical dimension increases from 2 to 2^3 . This means of course that the computational complexity is now bigger compared to the usual case with a lower physical dimension.

Starting from this approach we can formulate the corresponding Hamiltonian which describes the Heisenberg interaction on the kagome for the square lattice and use this to calculate the ground state. This new

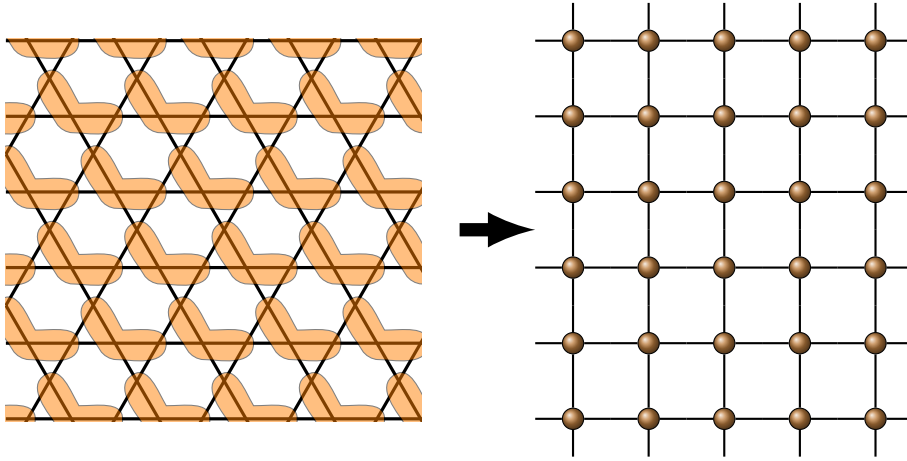


Figure 7.1: Mapping scheme from the kagome to the square lattice. We combine the three orange marked spins together and end up with a square lattice. One single link in the square lattice corresponds to two links in the kagome lattice. Since all nearest neighbours in the kagome lattice are mapped to either one single site or nearest neighbours in the square lattice, the interaction remains local.

Hamiltonian on the square lattice is still local with only nearest-neighbour interactions. Additionally we choose a 2×2 unit cell on the square lattice for our calculation. Hence we have a unit cell of six sites on the kagome lattice and perform the simple update for the square lattice to obtain the ground state via imaginary time evolution. From this we calculate the expectation values, e.g. of the energy per lattice site, via the CTM or HOTRG algorithm.

Of course this is not the only mapping scheme from the kagome onto the square lattice. Another possible mapping would be combining all up-triangles to one lattice site (see sec. A.3). This would however result in a next-to-nearest neighbour interaction which is not easy to implement in the algorithms used in this thesis.

7.2 GROUND STATE ENERGY

Before calculating the ground state energy for different bond dimensions it is useful to check how large the bond dimension of the environment should be chosen. We therefore plot the convergence of the ground state energy depending of the bond dimension χ on the environment (see fig. 7.2). The behaviour of E_0 depending on χ is a priori not clear. It is possible that the energy decreases continuously with increasing χ , but also that convergence is reached and the value saturates. Also from numerical instabilities it is possible that the energy increases although a larger χ is used.

In our case, it is plainly visible that the environment converges very fast already for small values of χ . In figure 7.2 the ground state energy did already converge for $\chi = 10$ for a bond dimension of the PEPS of

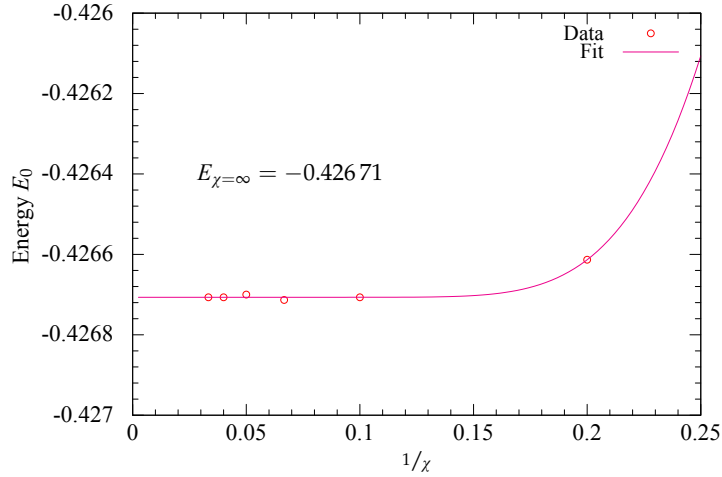


Figure 7.2: Convergence of the ground state energy depending on the bond dimension of the environment. The bond dimension of the corresponding PEPS was $D=3$. To show the very fast convergence of the ground state energy we perform an exponential fit. From the scaling towards $\chi \rightarrow \infty$ we see that with $\chi = 15$ we have already almost completely converged.

$D = 3$. Since it is possible that for higher bond dimensions of the PEPS a slightly higher χ is needed we choose $\chi = 15$ for the calculations of the ground state energies for all D .

The results of our calculations of the ground state energy for a converged χ are only upper bounds for the true ground state energy. The reason for this is that we only have an approximate ground state as well as only an approximating method for calculating the expectation value. Thus we are not able to give the exact ground state energy of the model, but, due to the variational principle (see sec. 2.4), an upper bound.

Now we calculate the ground state energies of this model for different bond dimensions of our PEPS. The resulting energies can be seen in table 7.1. We calculated the ground state energy with our CTM algorithm as well as the HOTRG algorithm. The lowest ground state energy we find directly with our method is at a bond dimension of $D = 9$ with $E_0 = -0.43447$ via the CTM algorithm. This however was not the calculation with the highest bond dimension since a calculation with $D = 10$ was performed, too. For this large bond dimension we were not able to calculate the expectation value with $\chi = 15$ due to limited computational resources. The environmental bond dimension was therefore reduced to $\chi = 10$. This could be the reason why the energy of this calculation is worse than for $D = 9$. The best ground state energy we are able to obtain with our method is therefore $E_0 = -0.43447$ at $D = 9$.

Of course this result is still biased due to a finite bond dimension. To get rid of this effect we try to extrapolate from our data to $D \rightarrow \infty$. Based

	PEPS D	Env χ	Energy
CTM	2	15	-0.419 49
	3	15	-0.426 71
	4	15	-0.429 96
	5	15	-0.431 12
	6	15	-0.433 19
	8	15	-0.434 05
	9	15	-0.434 47
	10	10	-0.434 13
HOTRG	2	15	-0.416 40
	3	15	-0.424 87
	4	15	-0.430 84
	5	15	-0.432 80

Table 7.1: Ground state energies of the spin-1/2 Heisenberg model on the kagome lattice.

on the behavior of our data we assume an exponential behavior for E_0 depending on D . We plot the energy against the bond dimension for each of the used methods and try to perform a fit with an exponential curve (fig. 7.3). The resulting fit for the values obtained via the CTM algorithm does not improve the ground state energy by a big margin for the scaling towards infinity. It seems like the ground state energy has already converged and that we have already obtained the best possible state with our method.

In the case of the HOTRG algorithm it is noteworthy that for small values of $D < 4$ the results lie above the energies obtained by the CTM algorithm, however for $D \geq 4$ the resulting energy is lower. The fit therefore shows a steeper behavior within the scaling towards infinity which ultimately results in a lower ground state energy for large bond dimensions. This fit however is not as trustworthy since only four points exist from which this behavior was extrapolated. It might be that the tendency of the real data is not as strong as the fit suggests or even that the decay does not follow an exponential curve. Nevertheless we used an exponential curve for this fit since it decreases quicker than any polynomial. Thus it should give an upper bound to the ground state energy. However, since we only have access to very few points, one should be careful with trusting this value.

It is not known why the HOTRG gives higher energies for small bond dimensions but lower ones for large D .

Now we want to compare our results with other methods and their results. The ground state energies of all the different methods are shown in figure 7.4. From this plot we can see that our ground state energy

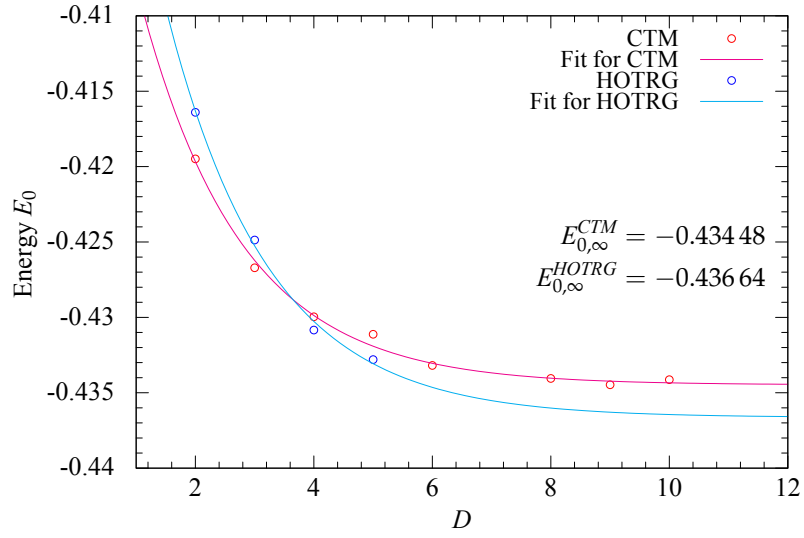
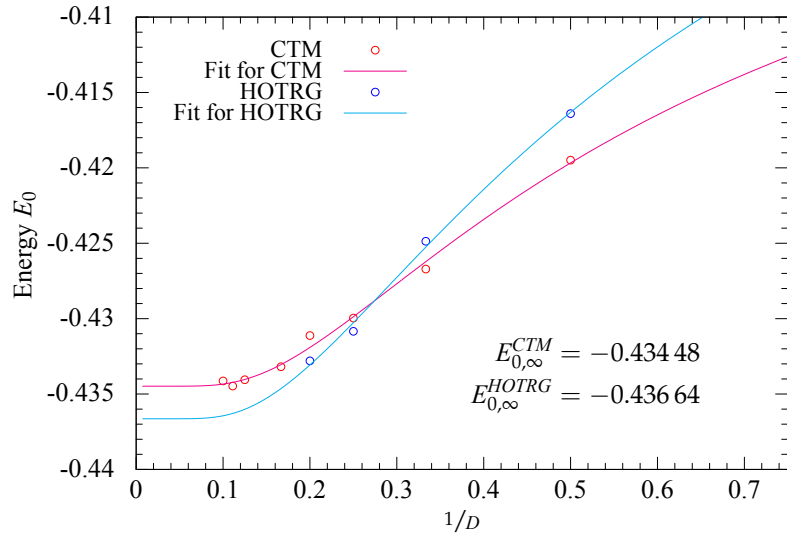
(a) E_0 depending on D (b) E_0 depending on $1/D$

Figure 7.3: Scaling to an infinite bond dimension from the obtained data. We fit the data obtained by the CTM and the HOTRG algorithm (see table 7.1) separately with exponential curves of the form $f(x) = ae^{-bx} + E_{0,\infty}$. From this we extract the ground state energy at infinite bond dimension. Additionally we plot the results against $1/D$.

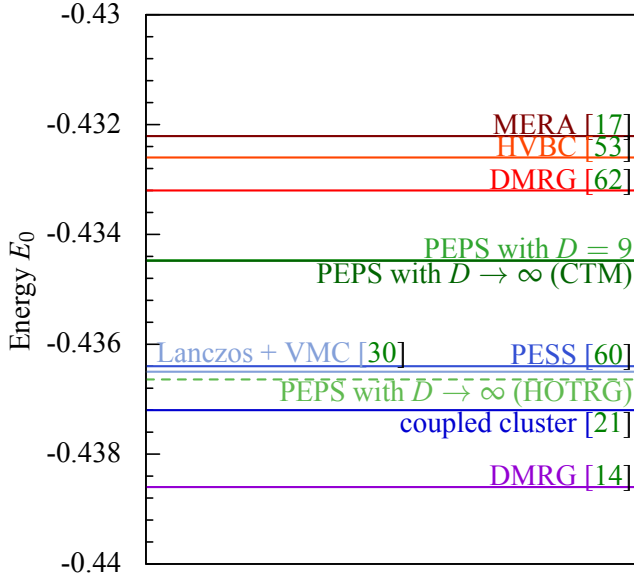


Figure 7.4: Comparison of our results with other methods. Our upper bound for the ground state energy is in very good comparison with the energies obtained by other methods.

is well comparable with the results found by other methods. We are below the energies found by MERA [17] and HVBC (honeycomb valence bond crystal) [53] as well as an upper bound from a DMRG study which was applied directly to an infinite 2D system [62]. However there are also methods which yield lower ground state energies like an extensive DMRG study with an intrinsic $SU(2)$ spin symmetry and a bond dimension of 16 000 [14].

Another interesting method is the *projected entangled simplex state* (PESS) ansatz [60]. This is a similar ansatz to our PEPS approach. Such PESS states are a representation of simplex solid states within the lattice. Therefore all lattice sites which are part of a simplex are joined by an *entangled simplex tensor* which describes the correlation of the particles within each simplex. The size of such a simplex can be chosen depending on the corresponding system. If the simplex consists of N particles the state is called a N -PESS. For $N = 2$ this state is equivalent to a normal PEPS. The lowest ground state energy by this method was found by a 9-PESS which was the corresponding simplex state consisting of three up-triangles with a bond dimension of 13. Unfortunately we are not able to address bond dimensions of this sizes to give a closer comparison to these results. However for the bond dimensions that we can access we are very close to the ground state energies which have been found by this method. If we compare their results with the scaling of the HOTRG results, it is worth mentioning that our ground state energy is even slightly lower.

7.3 NATURE OF THE GROUND STATE

Even if our ground state energy is in good comparison with other methods, it is still an open question if our ground state has the form of a quantum spin liquid. Not every method in this region found a spin liquid at the ground state, some also find some sort of valence bond crystal.

To check if the ground state really is a spin liquid and no other state, one would have to look at every symmetry of the model and the lattice and check that none of them are broken.

This, however, would be a very difficult task since there are many underlying symmetries within the lattice and Hamiltonian itself. Since we cannot check for every symmetry we will only calculate the energy of each link within the lattice. If every link carries the same energy we will conclude that the ground state is a possible QSL since it breaks no obvious symmetry. This is however only an indicator and we cannot say with absolute certainty that this state is in fact a QSL. In the case that the energy of the different links varies we can say that the state is no QSL but some sort of VBC with a certain structure which will be defined by the pattern of the energies within the lattice.

To give at least a suggestion of the nature of the ground state we will calculate the energy of each link within the lattice. We then plot the results in a so-called *bond strength map* by matching a specific width of the link between the lattice sites to a certain energy.

Since a VBC state has only short-ranged entanglement, it is expected that for low bond dimensions such a state is favoured over a QSL with long-ranged entanglement. This means that maybe a large bond dimension is needed to see a QSL in our ground state. Since we only have access to rather small bond dimensions, it is possible that we cannot see a QSL state. Thus, we will perform the calculation of the bond strength map for different bond dimensions of the PEPS to see if the structure of the energy changes depending on the bond dimension. From this we will hopefully see an emergent spin liquid or a specific VBC-structure. The resulting bond strength maps can be seen in figure 7.5. From the different bond strength maps for the different bond dimensions it is not easy to tell if a QSL will emerge at higher bond dimensions or not. It is clearly visible that the energy distribution over the lattice becomes smoother with a higher bond dimension and the difference between the strongest and weakest bonds decreases.

However if one keeps track of the development of the bond strength map depending on the bond dimension one notices that the difference between these maps is sometimes quite large and sometimes only marginally. The difference between $D = 2$ and $D = 4$ or $D = 6$ and $D = 8$ is very small as well as the development towards a more uniform picture of the energies. On the other hand the difference between $D = 4$ and $D = 6$ is quite large and clearly visible. This behaviour can also be seen in figure 7.6.

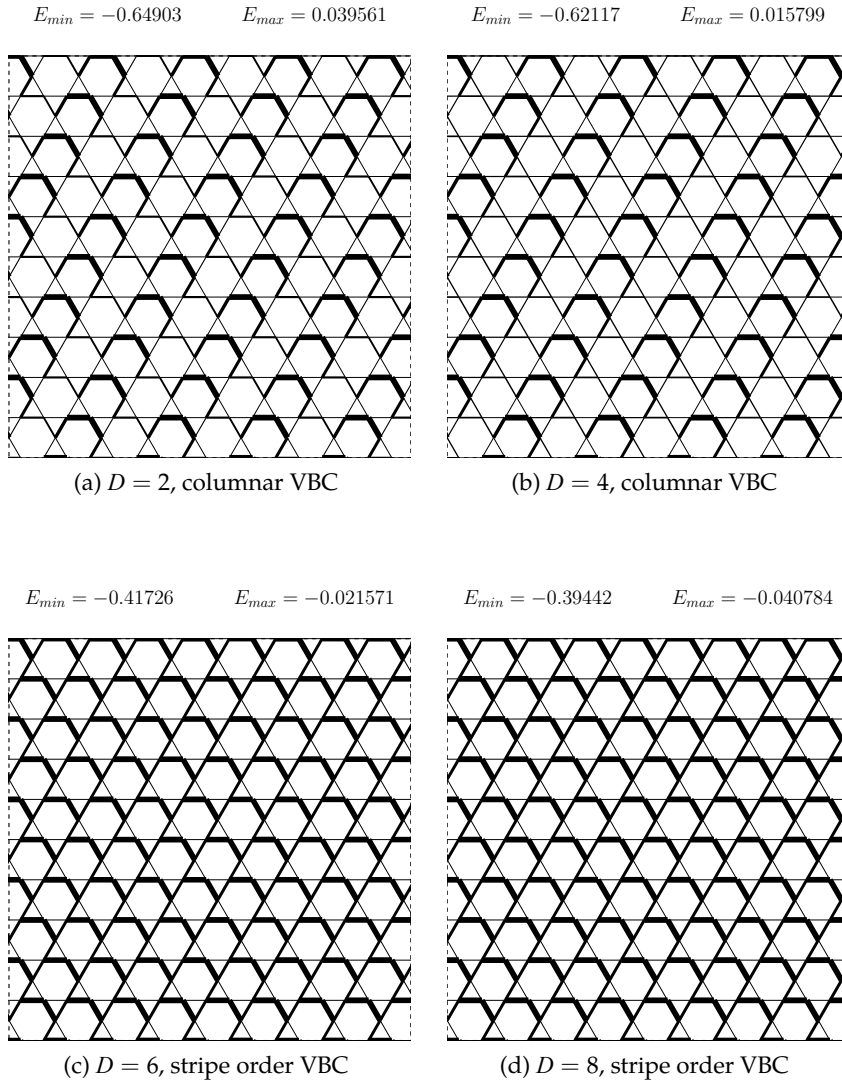


Figure 7.5: Bond strength map of the KAFM for different bond dimensions of the PEPS. At low bond dimensions a VBC-like structure arises which diminishes, but not completely vanishes, if D increases. From this it is hard to conclude if a QSL emerges at larger bond dimensions.

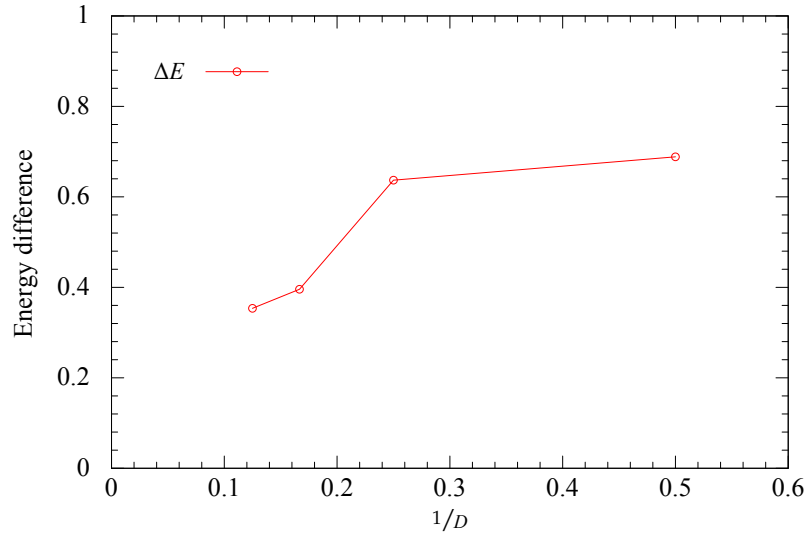


Figure 7.6: Energy difference between the strongest and weakest bond within the bond strength map depending on the bond dimension. Due to this sudden jump within ΔE it is not possible to give a prediction about the behaviour at infinite bond dimension.

The reason for this behavior is completely unknown and it is therefore extremely hard to give a prediction about the behaviour of the bond strength map at higher bond dimensions. One possibility would be that the PEPS with low bond dimension breaks the $SU(2)$ symmetry slightly and a larger D is needed to restore this symmetry. This could lead to such a jump in the difference of the minimal and maximal energy. It is however easily possible that at a later point another abrupt improvement takes place and the distribution of energy throughout the lattice becomes uniform. This would suggest that our ground state is a QSL. If the difference between the minimal and maximal energy saturates at some point we have a valence bond crystal with a certain order. Since it was not possible to go to higher bond dimensions we are not able to give a conclusive result for the nature of the ground state from our calculations.

The states we obtained with the bond dimensions accessible to us are closer to a valence bond crystal with a columnar order than to a QSL. It is also possible that this specific order within the bond strength map is a consequence of the chosen mapping between the kagome and the square lattice. Therefore different mappings might lead to different structures and are maybe better suited to encompass a QSL.

7.4 KAFM WITH A MAGNETIC FIELD

In addition to the ground state properties of the spin- $1/2$ Heisenberg model we are also interested in the behavior under an external mag-

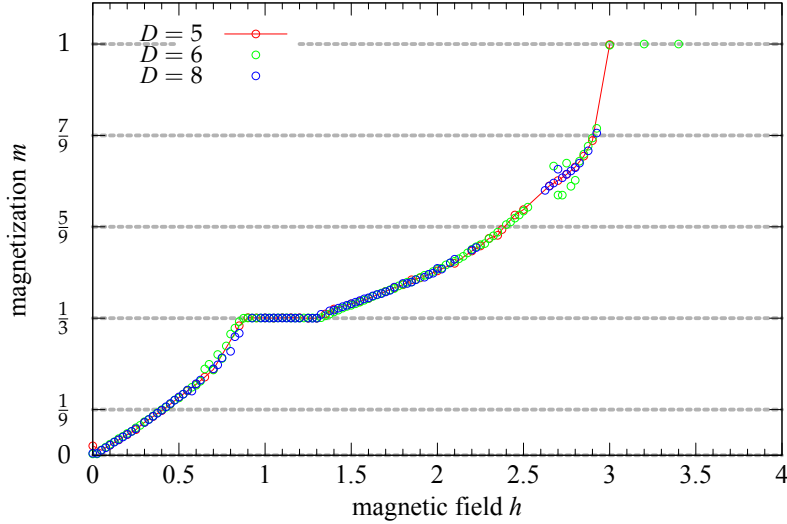


Figure 7.7: Magnetization curve of the kagome Heisenberg antiferromagnet with an external magnetic field. The plateau at a $1/3$ magnetization is clearly visible, as well as the jump to saturation at a field strength of $h = 3$.

netic field. The interaction with an external magnetic field modifies the Hamiltonian to

$$\mathcal{H} = \sum_{\langle ij \rangle} \vec{S}_i \vec{S}_j + \sum_i h \cdot S_i^z. \quad (7.1)$$

We will now calculate the ground state for different values of h and look at the corresponding magnetization of a triangle within the lattice.

The behavior of the magnetization is still topic of recent discussions and not completely understood. Recent studies show a highly possible plateau at a $1/3$ -magnetization and a jump of the magnetization from $7/9$ to 1 at the saturation field of $h = 3$ [7, 28, 40].

Some papers additionally suggest some more plateaus at a magnetization of $1/9$, $5/9$ and $7/9$ [40] which are however not found by every method.

From the experimental side a full examination of this model is still to be done. However it is noteworthy that a plateau close to $1/3$ has recently been found in two different spin- $1/2$ kagome compounds[43].

Due to this we want to calculate the magnetization behavior with our PEPS approach and search for these plateaus.

From our calculations (see fig. 7.7) we can clearly see the plateau at a magnetization of $1/3$ which was found by many methods. Within this plateau the “spin compressibility” (the derivative of the magnetization with respect to the magnetic field) vanishes and hence this phase can be seen as incompressible.

A similar plateau has been seen for the triangular lattice [38]. In this case the corresponding ground state consists of a $\uparrow\uparrow\downarrow$ -structure on the

triangular plaquettes. This state is of course still infinitely degenerate due to the infinite amount of tiling patterns on the triangular lattice. Since on the triangular lattice the frustration has a similar role as on the kagome lattice, the same mechanism should also be valid here. In analogy the plateau of the KAFM should also consist of the $\uparrow\uparrow\downarrow$ tiling structures. This should also be visible within the bond strength map of the corresponding system, since the link between the anti-aligning spins will have a much lower energy than the link between two parallel spins. This means that a $\uparrow\uparrow\downarrow$ -structure manifests in the bond strength map by two strong and one weak link within each triangle.

If we plot the bond strength map for a ground state within this plateau we find exactly the expected pattern of two strong bonds and one weak bond within every triangle (figure 7.8). We additionally calculated the expectation value of the magnetization on each site of a triangle separately and displayed the results also in figure 7.8. We can see that the expectation values are positive on two sites and negative on the last site. This confirms the $\uparrow\uparrow\downarrow$ -structure already suggested by the structure of the bond strength map.

We therefore can verify the existence of the plateau and its nature with our TN based methods. The size and position of this plateau are also in very good agreement with all other methods.

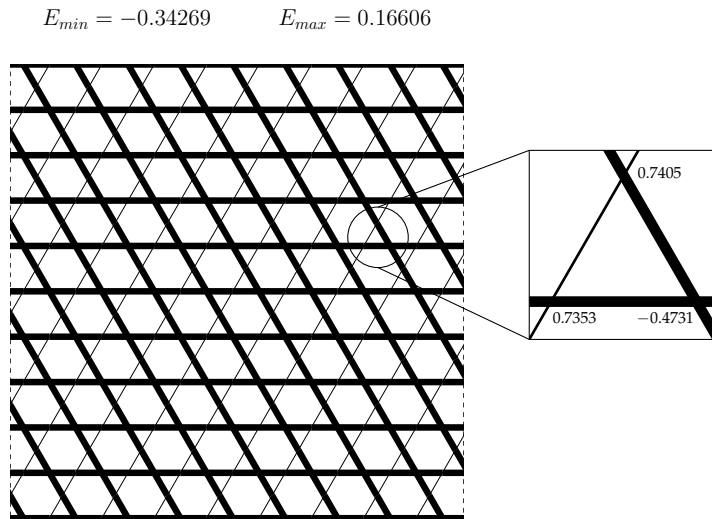


Figure 7.8: Bond strength map at the magnetization plateau at a magnetic field of $h=1$. The strength of the bonds in the lattice show a certain order of stronger and weaker links. The weaker links are a sign for neighbouring parallel spins whereas the stronger links suggest anti-parallel spins. From this we can conclude that each triangle consists of two up and one down spin. Additionally we calculated the single site expectation value for each site within a triangle to show that we find two spins with very similar spin with equal sign and one spin with a different sign which verifies the expected $\uparrow\uparrow\downarrow$ structure.

Additionally we also find the same saturation behavior at a magnetic field of $h = 3$ as well as the same characteristic jump to this saturation from a magnetization of $m = 7/9$. All these features have been observed by all previous methods. However we were not able to find the additional plateaus which are not present in all previous studies with different methods. In a study by Hida[28] it was claimed that these plateaus only exist in the case of some sort of distortion within the lattice. This could be the reason why we do not see the effect since our calculation is only valid for uniform infinite size two dimensional systems without finite-size effects, unlike previous methods.

This however would mean that other methods like [7] or [40] would have some sort of distortion of the model within their approach or suffer from some finite-size effects.

THE SPIN-1 KAGOME HEISENBERG ANTIFERROMAGNET

Additionally to the study of the spin-1/2 KAFM (chap. 7) we had a closer look at the spin-1 kagome Heisenberg antiferromagnet. In contrast to the spin-1/2 case, there are not as many studies about the corresponding ground state of this model even though there are several candidates for such a system in nature. For example $\text{KV}_3\text{Ge}_2\text{O}_9$ [24] and $\text{BaNi}_3(\text{OH})_2(\text{VO}_4)_2$ [19] are reported to be good candidates for spin-1 antiferromagnets with a kagome geometry.

Hida [29] proposed a hexagonal singlet solid (HSS) as the ground state, based on an exact diagonalization calculation. This is a translationally invariant state in which all spin-1's can be seen as two spin-1/2's projected into the spin-1 subspace and then all spin-1/2's on a hexagon within the lattice form a singlet.

Other methods claim that the ground state is some kind of *simplex solid*. This means that there are geometric regions which are stronger connected than others. In [8] it was proposed that the ground state undergoes some kind of trimerization, which means that the up- and down-triangles within the lattice carry different energies (fig. 8.1) and thus the C_2 -symmetry between these triangles is broken. The resulting state is known as a *simplex solid*. Such phases, which break point group symmetries, are named *nematic* and are characterized by fractional magnetization plateaus [49]. These plateaus are called incompressible since the spin compressibility vanishes inside these plateaus.

If we add a magnetic field with on site interaction to the model and see magnetization plateaus within the magnetization curve, we also expect that the corresponding ground state at $h = 0$ shows this kind of trimerized nematic phase.

Another ground state that was proposed is a *resonating AKLT-loop* (RAL) state [33]. This spin liquid state is a superposition of all possible AKLT-loops on the kagome lattice and seemed very promising because it had a slightly lower energy than the HSS for small system-sizes. However,

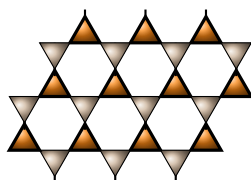


Figure 8.1: Trimerization within the kagome lattice. The up and down triangles carry different amount of energies and build a so called *simplex solid*

in the thermodynamic limit the resulting energy is much higher. Thus this state has again been discarded as a very likely ground state of this model.

8.1 GROUND STATE ENERGY

For our calculations we choose the same approach as before, which means that we use the iPEPS algorithm for the square lattice with the simple update. We therefore perform the same mapping as described in section 7.1 to get from the kagome onto the square lattice. This increases the effective physical dimension of our model on the square lattice to $3^3 = 27$, which is already quite large.

We calculate the ground state again by performing an imaginary time evolution with the simple update and display the resulting ground state energies per lattice site for different bond dimensions in table 8.1. The ground state energies were again calculated with the CTM as well as the HOTRG algorithm. Since it is not expected that the convergence of this model differs much from the spin-1/2 case we choose again the same environmental bond dimension of $\chi = 15$.

	PEPS D	Env χ	Energy
CTM	2	15	-1.1623
	3	15	-1.1773
	4	15	-1.1841
	5	15	-1.1869
	6	10	-1.1885
	7	5	-1.1891
HOTRG	2	15	-1.1609
	3	15	-1.1780
	4	15	-1.1872
	5	15	-1.1875

Table 8.1: Ground state energies per lattice site for the spin 1 heisenberg model on the kagome lattice.

From our obtained results we again try to determine the limit for large bond dimensions. Hence we plot the ground state energy against the bond dimension and perform an exponential fit as before (see sec. 7.2). The fit with the resulting ground state energy for the large D scaling can be seen in figure 8.2. From our data and the corresponding fit we can see that we obtain a ground state energy which is $E_0 = -1.1893$ if we perform the scaling towards an infinite bond dimension of the data obtained by the CTM algorithm. It is noteworthy that we only have ac-

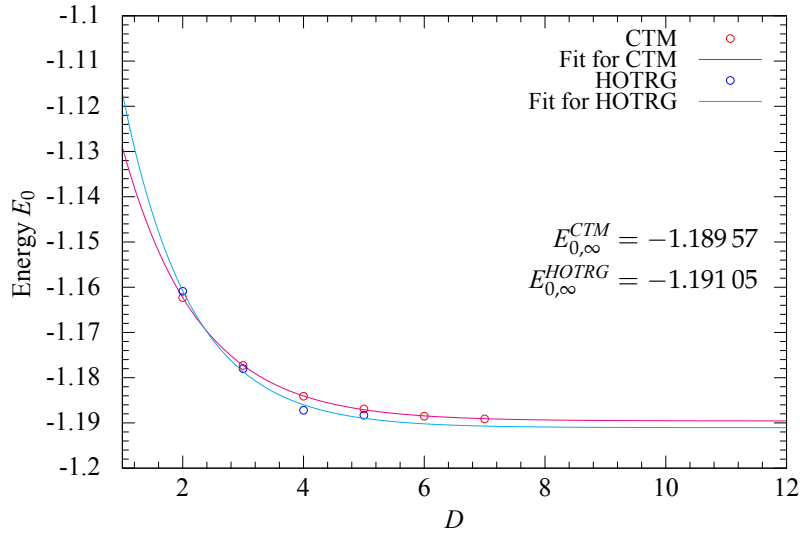
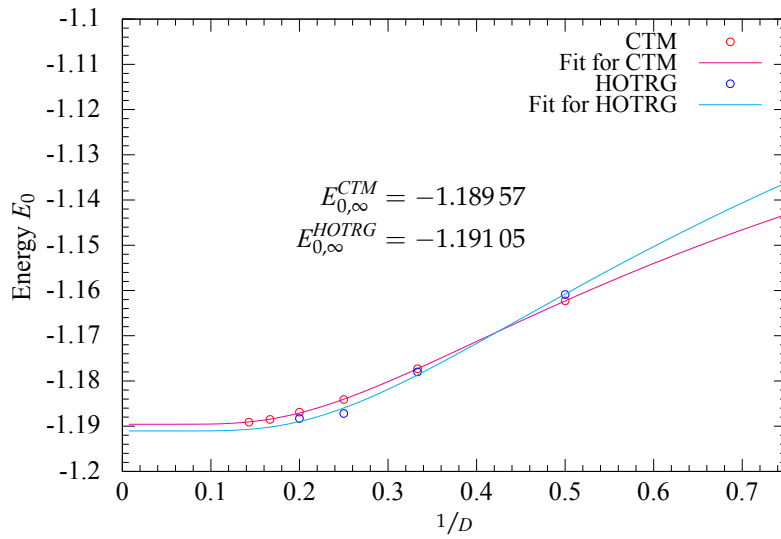
(a) E_0 depending on D (b) E_0 depending on $1/D$

Figure 8.2: Scaling to an infinite bond dimension from the obtained ground state energies. We perform the fit with an exponential curve $f(x) = ae^{-bx} + E_{0,\infty}$. We fit the results from the CTM and the HOTRG algorithm separately and plot the result once against D and once against $1/D$

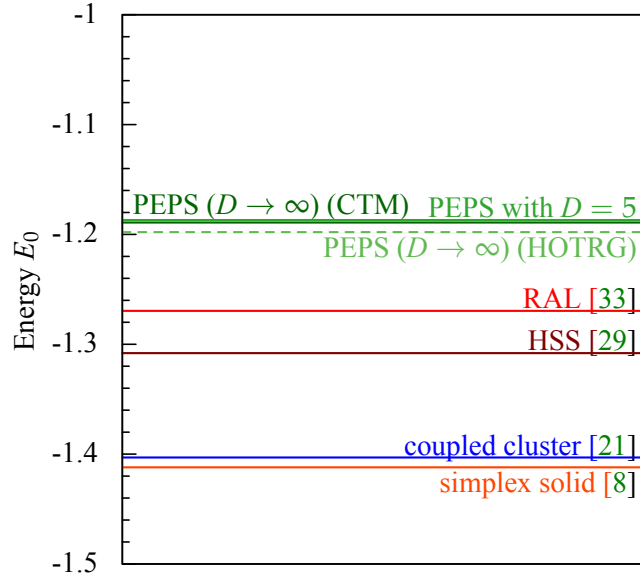


Figure 8.3: Comparison of the results obtained by our method and the results of other methods.

cess to much smaller bond dimensions compared to the spin- $1/2$ KAFM model. The reason for this is that the physical dimension here is much larger which increases the computational time and resources needed for finding the ground state.

The fit of the ground state energies obtained by the HOTRG algorithm gives a very similar limit of the energy for $D \rightarrow \infty$. The resulting limit of $E_0 = -1.1911$ is slightly lower compared to the fit of the CTM-data, however we have access to less data points to perform this fit and it is therefore less trustworthy.

We now want to compare the values we obtained with our method to other numerical methods and their ground state energies. To allow for an easy comparison, we show all the ground state energies from the different methods within one plot. The resulting graph can be seen in figure 8.3. We can see that the energy found by our method is higher than the results from other methods. All proposed ground states, like the resonating AKLT-loops (RAL) [33] or simplex solid [8], provide a lower ground state energy than our calculation. The best ground state energy found so far by a simplex solid state lies at $E_0 = -1.412$ which is much lower than the $E_0 = -1.1893$ we were able to obtain with the CTM algorithm. Even the resulting energy from the rather optimistic fit of the HOTRG results is still notably higher than the energies of all the proposed ground states.

It is not known why our method fails to give a good estimate of the ground state energy of this model, especially since the estimate for the spin- $1/2$ KAFM was very good. It is of course possible that the behavior of the ground state energy at higher bond dimensions is different from the expected exponential behavior. It may be that the energy decrease

is stronger above a certain bond dimensions and the real exponential behavior starts in a later region which is not accessible to us. In addition to an insufficient bond dimension, it might be that the mapping between the kagome and the square lattice is not optimal for the spin-1 KAFM. As explained before, it was proposed that the ground state exhibits some sort of trimerization which results in a simplex solid state and it is quite possible that the specific mapping chosen in this thesis is not able to encompass such a trimerized state. A different mapping (like in sec. A.3) might be a better ansatz to find such a state.

Another possibility is that this state is not accessible with the simple update which was used in our calculations. If the correlation length within the ground state is large, the simple update is not able to give an accurate representation and the full update is needed for a better description. Also the enlargement of the unit cell might help to obtain better energies from our calculations.

The exact reason for the mismatch of our method and all the others cannot be pinned down but it is most likely one or more than one of the reasons listed above.

8.2 NATURE OF THE GROUND STATE

Now we try again to give a suggestion about the nature of the obtained ground state. As stated previously, it was suggested in [8] that the ground state forms a simplex solid which manifests in a trimerization. A trimerized state is easily visible within the bond strength map since the links in certain triangles will be stronger than in other triangles. We will now check if we can reproduce this result with our method even though we do not expect to see it within our ground state. The reason for this is that the proposed energy of a simplex solid within the spin-1 KAFM has a much lower energy than the ground state energy which was found with our method.

Nevertheless we calculated again the energy of each link within the lattice and plotted the results in a bond strength map (see fig. 8.4). We performed the calculations again for different values of the bond dimension of the model to see if some structure emerges with a larger D . However within the bond strength maps of the bond dimensions that are accessible with our method we are not able to see any specific pattern emerging which would suggest a simplex solid state within the lattice. The energies of the bonds within the triangles do not vary depending on the fact that the triangle is an up- or down-triangle.

As stated before, these results are expected since our ground state energy differs much from the results obtained by simplex solid states. From the structure we see within our data it is difficult to give a conclusive suggestion towards the nature of this ground state.

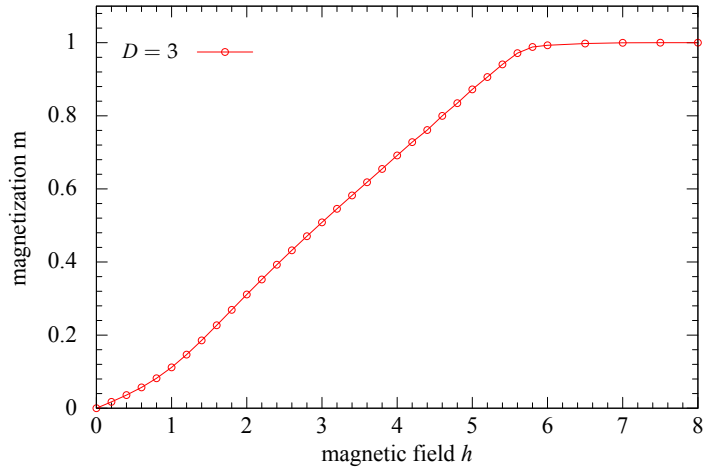


Figure 8.5: Magnetization curve of the spin-1 Heisenberg antiferromagnet on the kagome lattice. No plateau is visible within this curve and we therefore cannot reproduce the results from [28, 49].

reasons, like the use of the simple update, the choice of the mapping or the size of the unit cell have already been discussed.

THE SPIN- $3/2$ KAGOME HEISENBERG ANTIFERROMAGNET

The Heisenberg model on the kagome lattice is subject to many studies, especially for small values of the spin (see chap. 7 and 8). For higher spins the amount of theoretical studies decreases and only very few exist in the case of $s = 3/2$. This model however is still very relevant and interesting since it occurs naturally within several mineral compounds. One of these is chromium-jarosite ($\text{KCr}_3(\text{OH})_6(\text{SO}_4)_2$) which has a perfect kagome structure and an antiferromagnetic interaction with spin- $3/2$ [44]. Moreover the large-spin limit is interesting for observing the quantum-classical transition.

Although these compounds exist, there are almost no theoretical studies concerning this model. There was only a higher spin examination with a coupled cluster approach [21], which gave an estimate of the ground state energy, an early spin-wave analysis [9], which suggested that the ground state may support long-range magnetic order, and a large- N expansion of the model [51], which suggests a quantum-disordered ground state. This means that there are two different ground states supported by different theoretical approaches.

From the experimental side the question about the nature of the ground state could not be answered in a final matter either. Several spin- $3/2$ antiferromagnetic kagome compounds, like $\text{SrCr}_{9-x}\text{Ga}_{3+x}\text{O}_{19}$ [56] and $\text{Ba}_2\text{Sn}_2\text{Ga}_3\text{ZnCr}_7\text{O}_{22}$ [22], seem to have no antiferromagnetic order in their ground state, but undergo a spin-glass transition. However both of these compounds have a slightly distorted kagome structure whereas chromium-jarosite has no distortion and shows no spin-glass transition, but a long-range magnetic order. This means that there is evidence for both disordered and magnetically ordered states, from both the experimental, as well as the theoretical side. Thus the nature of the true ground state is not yet known.

Due to this lack of theoretical and numerical results for the spin- $3/2$ KAFM we will now try to examine this model more closely with our PEPS approach. We therefore perform again the same mapping between the kagome and the square lattice as before (see sec. 7.1). Hence the physical dimension of the model on the square lattice is $4^3 = 64$ which is very large. Since the simple update scales with d_{phys}^4 , this large physical dimension restricts us to very small bond dimensions of the PEPS, due to the available computational resources.

9.1 GROUND STATE ENERGY

We again approximate the ground state of this model via the iTEBD algorithm and calculate the expectation value of the corresponding ground state energy with the HOTRG and the CTM algorithm. In this case it is noteworthy that the HOTRG algorithm is a very useful method to calculate expectation values, due to the fact that the algorithm does not scale badly with the large physical dimension of this model.

	PEPS D	Env χ	Energie
CTM	2	15	-2.7295
	3	15	-2.7894
	4	15	-2.7977
	5	5	-2.8002
HOTRG	2	10	-2.7367
	3	10	-2.7887
	4	15	-2.8017
	5	15	-2.8027

Table 9.1: Ground state energy of the spin- $3/2$ antiferromagnet on the kagome lattice. Due to the large physical dimension of this model it was not possible to go to higher bond dimensions than $D = 5$. In the case of $D = 5$ it was only possible to choose $\chi = 5$, because a larger χ would exceed the available memory. One should also notice that the obtained ground state in the case of $D = 5$ was not yet fully converged at the time the expectation value was calculated. However we included it anyways since it already gives us a lower ground state energy.

The resulting expectation values can be seen in table 9.1 for all bond dimensions which were accessible with the computational resources available. Since there are not many other theoretical or numerical studies of this model we can not give a good comparison of our results with other methods. The only published value was obtained by a coupled cluster treatment [21] which is at $E_0 = -2.835$. Additionally there was a very recent unpublished calculation by Poilblanc & Picot with the same method as in [49] which results in a ground state energy of $E_0 = -2.783$.

Before we give a closer comparison with these results we perform a scaling towards infinite bond dimension (see fig. 9.1). The problem with the scaling is that we only have access to very few bond dimensions and thus very little data to perform the exponential fits. It is therefore quite possible that the scaling towards an infinite bond dimension does not encompass the correct behaviour. However, from the fit one

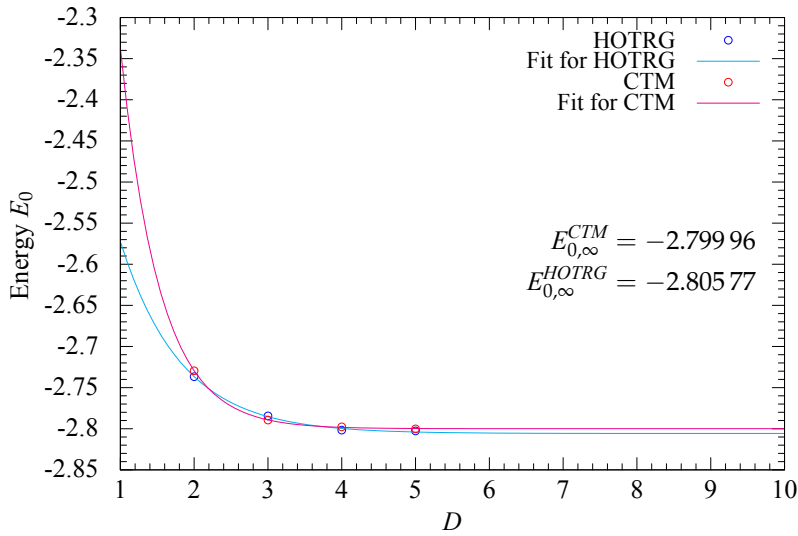
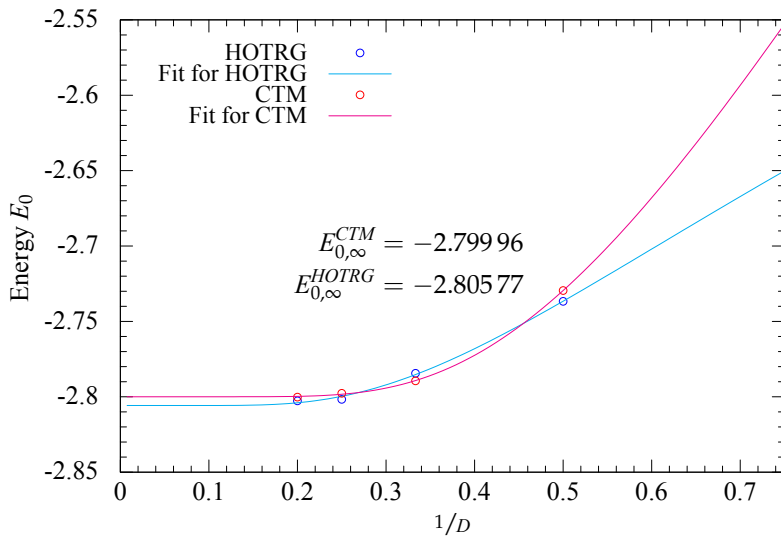
(a) E_0 depending on D (b) E_0 depending on $1/D$

Figure 9.1: Scaling towards infinite bond dimension for the spin- $3/2$ KAFM. As in the spin- $1/2$ case we fit with $f(x) = ae^{-bx} + E_{0,\infty}$ and extrapolate the energy to infinite bond dimension. We plot the energy once depending on D and once as a function of $1/D$.

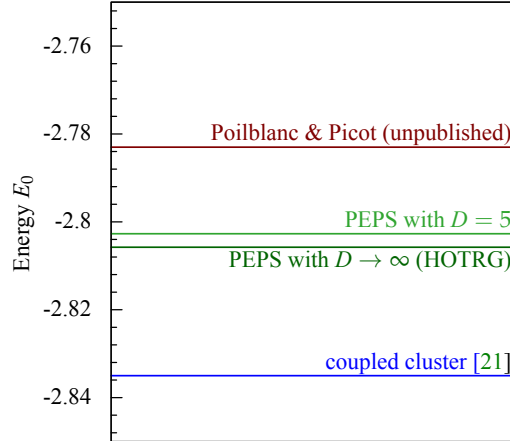


Figure 9.2: Comparison of the ground state energies of the spin- $3/2$ KAFM obtained by different methods.

could suggest that the calculated energy has already converged, because the energy for the infinite bond dimension is very close to the calculated one with finite D and the HOTRG algorithm. Even if this behaviour is not correct, it is reasonable to assume that this energy is reached at larger bond dimensions and we therefore suggest this as our upper bound for the ground state energy. If we look at the scaling from the energies obtained via the CTM algorithm one notices that the extrapolated ground state energy is even above the value we obtain directly with $D = 5$.

Additionally, one should mention that the ground state at $D = 5$ that was used to determine E_0 was not yet fully converged. Anyhow, due to the limited time available for this calculation, we decided to calculate and include the energy of this ground state. Nevertheless, this PEPS with $D = 5$ still gives lower results than the approximated ground states with lower bond dimension. It is therefore likely that we can get to even lower energies if we let the ground state fully converge.

The ground state energy we obtain from the scaling of the HOTRG data is $E_0 = -2.806$. To compare this result with the energies found by other methods, we plot once more all values of E_0 into one figure (see fig. 9.2). We can see that our results are in good agreement with the results obtained by Poilblanc & Picot and the ones from the coupled cluster approach [21].

9.2 NATURE OF THE GROUND STATE

To get a closer examination of the nature of the ground state we plot again the bond strength map (see fig. 9.3) for different values of the bond dimension of our PEPS. We can see that there is no real structure visible within these maps and also the pattern does not seem to change much with increasing bond dimension. However we only have access

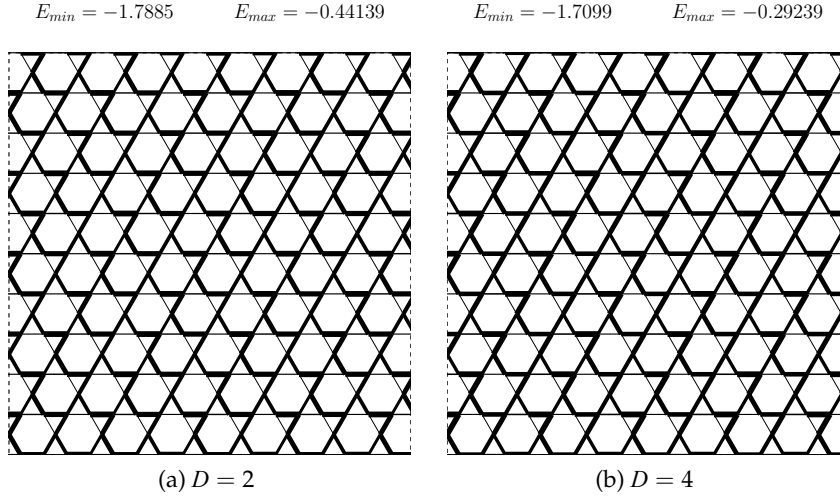


Figure 9.3: Bond strength map of the ground state of the spin- $3/2$ antiferromagnet.

to two different bond dimensions and the structure may change with a larger D .

It is very hard to determine the nature of the corresponding ground state from only the bond strength map as available data. The state displayed here could be some disordered quantum state which could be close to a spin-glass, but could also be part of a long-ranged magnetically ordered structure. With our calculations we are not able to differentiate between these two possible states.

9.3 SPIN- $3/2$ KAFM WITH A MAGNETIC FIELD

A recent experimental study of chromium-jarosite[44] looked at the magnetization process of this compound under an external magnetic field. It was found that the magnetization exhibits a plateau at a magnetization value of $m = 1/3$ of the saturation value. Within this study the magnetization curve was measured at different temperatures and it was observed that the width of the plateau changes with the temperature. In fact it decreases if the temperature is lowered. It was therefore concluded that this plateau stabilizes due to thermal fluctuations by an order-by-disorder mechanism [57] and it was not clear if this plateau will still survive at $T = 0$ K. However within the study they suggested that it will not be visible at $T = 0$ K.

From the theoretical side there is no study about the behaviour of this model under a magnetic field. There was only one calculation based on a classical model, which suggested that a $\uparrow\uparrow\downarrow$ -structure stabilizes below a certain temperature due to thermal fluctuations and that the size of the region, in which this structure appears, gets narrower at lower temperatures [64].

We will therefore determine the influence of an external magnetic field on the magnetization with our PEPS approach to give a numerical result regarding the existence of this plateau.

The transverse magnetic field modifies the Hamiltonian as before (see eq. (7.1)) by an additional term proportional to the field strength and S_z . Coming from this Hamiltonian we calculate the ground state for different values of the magnetic field h and calculate the expectation value of the magnetization. The resulting values can be seen in figure 9.4.

Our results show that the magnetization curve exhibits a small plateau in the region of $2.8 < h < 3.4$ with a magnetization value of $m = 1/3 \cdot m_{sat}$. This is therefore the first numerical evidence of the existence of a magnetization plateau within the spin- $3/2$ KAFM at $T = 0$ K. Thus we can conclude that this plateau may get wider due to stabilizing effects from thermal fluctuations, but it is intrinsically stable.

Additionally to this plateau at $1/3$ magnetization we can see a second plateau at $m = 0$ in the region of $0 < h < 1$. This plateau has not been observed within the experimental study of chromium-jarosite[44] and we are the first one to see this plateau.

These plateaus can again be seen as incompressible since the derivative of the magnetization with respect to the magnetic field (the spin compressibility) vanishes within the plateaus. After obtaining these results, these plateaus have also been verified independently by Poilblanc and Picot. We therefore started a collaboration with them on the topic of the spin- $3/2$ KAFM.

In figure 9.4 one can see that there are some data points missing in the region $5.5 < h < 8.5$. In this region we experienced some convergence issues of our algorithm. The reason for this is unknown and it is possible that after more steps with the simple update we would have gotten

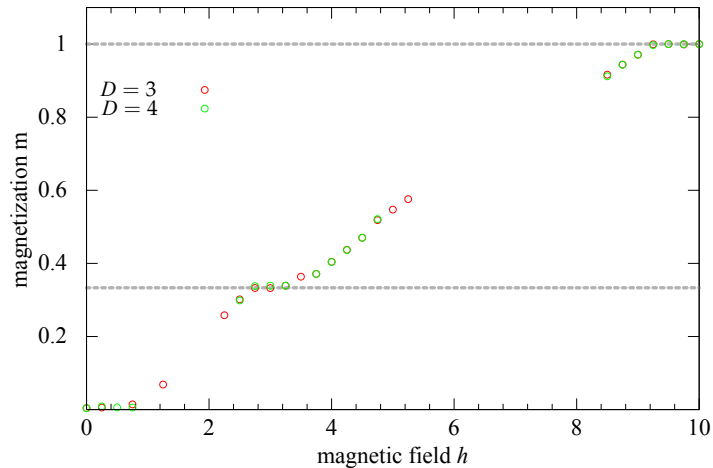


Figure 9.4: Magnetization curve of the spin- $3/2$ antiferromagnet in a magnetic field. It is clearly visible that we get a plateau with a $1/3$ magnetization. Some data $5.5 < h < 8.5$ points are missing, because of a lack of computational time to get a well-converged result.

an approximated TN ground state even in this region. However, due to the large physical dimension, the computational time needed for each step was so large that we were not able to finish the calculation within the given time frame.

$$E_{min} = -3.0637 \quad E_{max} = 2.0958$$

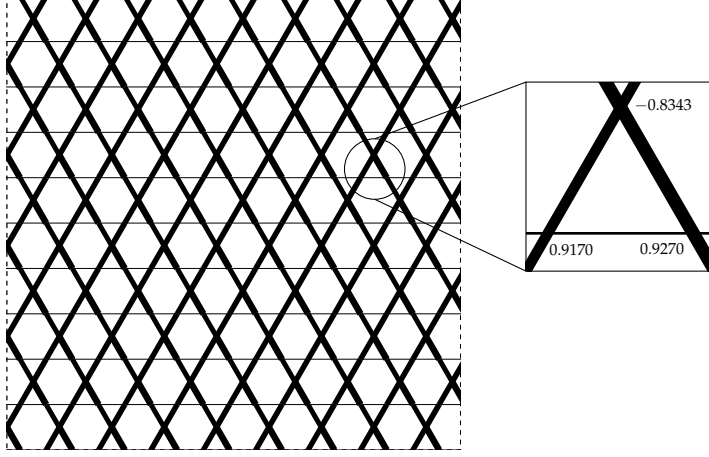


Figure 9.5: Bond strength map of the spin- $3/2$ KAFM within the plateau of the magnetization curve. We can see the expected structure of two strong and one weak link within each triangle. This is characteristic for the $\uparrow\uparrow\downarrow$ -tiling structure. We additionally calculated the expectation value of the magnetization on each lattice site within one triangle and normalized the values to the saturation magnetization. From this we can see that we have two parallel spins with equal sign and very similar magnetization and one spin antiparallel to them with different sign. This verifies the $\uparrow\uparrow\downarrow$ -structure of this plateau.

Now, that we concluded that the plateau exists at $T = 0$ K, we will check if the ground state in this region has the predicted $\uparrow\uparrow\downarrow$ -structure. Hence we plot again the bond strength map of this model and look for a structure with two strong and one weak bond within each triangle (see sec. 7.4).

As we can see in figure 9.5 we find the expected structure. Additionally we calculated the expectation value of the magnetization for each site of a triangle. The resulting values can be seen in the inset in figure 9.5. We can see that two of these expectation values have an equal positive sign and are linked by a weak bond, which means that they are parallel. The third spin has a negative sign and is linked with strong bonds to the other two spins which means that this spin is antiparallel to the other two. Thus we are able to verify the existence of a magnetization plateau as well as its proposed classical $\uparrow\uparrow\downarrow$ -structure.

CONCLUSION

In the first part of this thesis, we gave a general introduction to tensor networks, especially PEPS, and numerical algorithms based on them. In Part [ii](#), we benchmarked our algorithms with the two-dimensional Ising model on the square lattice, in the classical and in the quantum case. From this benchmark we concluded that the used algorithm (the so called simple update) is a good method to describe non-critical systems.

In Part [iii](#) we present our final results for the Heisenberg model on the kagome lattice for different values of the spin.

In chapter [7](#) we start with the spin- $1/2$ antiferromagnet and calculate the ground state energy, the magnetization under an external magnetic field and try to give a suggestion about the nature of the ground state. We find a ground state energy of $E_0 = -0.43447$, which is in very good comparison with many other methods. *This result is in fact amongst the lowest truly two-dimensional results for this model.*

There are currently two different states which are very good candidates as ground states of this model, the valence bond crystal and the quantum spin liquid. The lowest ground state energies are currently obtained by a QSL, which is also supported from experimental results. From the results obtained in this thesis it was not possible to conclude which of these states is the true ground state, since we find a VBC at the bond dimensions that are accessible to us, but it seems like a QSL might emerge at higher bond dimensions.

Additionally, we studied the magnetization of this model, since it was proposed that it exhibits one or more plateaus within the magnetization curve as a function of an external field. We were able to verify the existence of the plateau at $1/3$ of the saturation magnetization. Other proposed plateaus were not visible within our calculations.

Afterwards we studied the spin-1 Heisenberg antiferromagnet (chapter [8](#)) and also determined the ground state energy, its nature and the magnetization process. For this model we were not able to reproduce the results found by other methods. The ground state energy we obtained was way above the best results found by a simplex solid. Also the proposed trimerized ground state was not visible in our results, neither was the proposed magnetization plateau at a magnetization of $m = 1/3$. It is not clear why our approach fails in the case of the spin-1 model whereas it works very good for spin- $1/2$. It might be that this model requires the use of the full update instead of the simple update, a larger unit cell or simply a larger bond dimension.

Finally, in chapter 9, we studied the spin- $3/2$ Heisenberg model on the kagome lattice. This model has not been subject to a lot of previous studies. We therefore try to give an estimate of the ground state energy and examine the magnetization process.

We find a ground state energy of $E_0 = -2.788$. This result is in good comparison to a coupled cluster study [21] and another unpublished result. An experimental examination of this model suggested the existence of a $1/3$ magnetization plateau at finite temperatures, which seems to stabilize due to thermal fluctuations and it was concluded that this plateau was not likely to survive at $T = 0$ K. From the theoretical and numerical side there were no results on this process yet. Thus, we tried to look for the existence of this plateau at $T = 0$ K and in fact were able to see such a plateau within our results. We can therefore conclude that this plateau is intrinsically stable and does not depend on thermal fluctuations.

These recent results about the spin- $3/2$ KAFM led to a collaboration with Poilblanc and Picot which will also lead to a paper within the following months.

To summarize all the results obtained in this thesis all important findings are combined in table 10.1.

SPIN	E_0	D, χ	METHOD	PLATEAU
$1/2$	-0.434 47	9,15	CTM	$1/3$
	-0.432 80	5,15	HOTRG	
	-0.434 48	∞	scaling	
1	-1.1891	7,5	CTM	\times
	-1.1875	5,15	HOTRG	
	-1.1896	∞	scaling	
$3/2$	-2.8002	5,5	CTM	$0, 1/3$
	-2.8027	5,15	HOTRG	
	-2.8058	∞	scaling	

Table 10.1: Summary of all results obtained in this thesis

LARGE-S LIMIT

Now that we gathered the ground state energy for the Heisenberg model on the kagome lattice for different spins we want to determine the behaviour of the energy depending on the spin as a final and summarizing task. From standard linear spin-wave theory it was concluded that $E_0/s^2 = -1 - 0.4412/s$ [25] and thus that in the classical limit $\lim_{s \rightarrow \infty} E_0/s^2 = -1$.

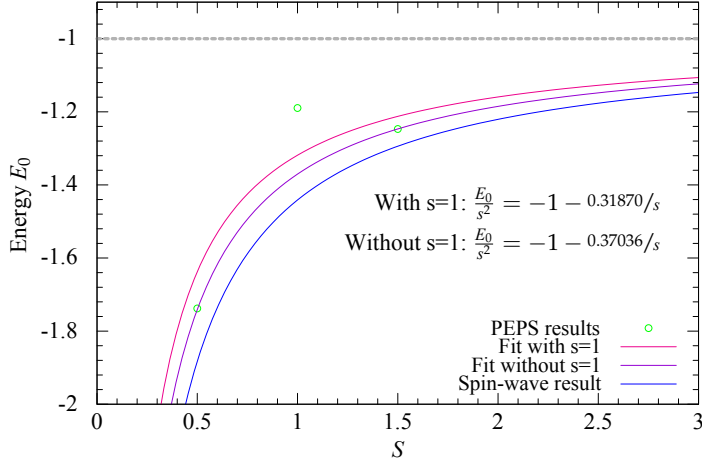


Figure 10.1: Behaviour of the ground state energy depending on the spin of the Heisenberg model. We fit with the predicted behaviour of $f(s) = -1 - a/s$, which was suggested by a linear spin-wave analysis of this model. We find that our results reproduce this behaviour except for the point at $s = 1$ which is known to be not very accurate.

Hence we plot our resulting ground state energies divided by s^2 and fit with $f(s) = -1 - a/s$ which is shown in figure 10.1.

From the resulting figure we can again see that our result of the ground state energy of the spin-1 KAFM is not in a very good agreement with the expected value. If we neglect this single point and only use the remaining two we can see that we can reproduce the $1/s$ -behaviour of E_0/s^2 and also the corresponding prefactor of $1/s$ is with $a = -0.3704$ in a similar region as the spin-wave result.

OUTLOOK

The main goal in the near future is to improve the results for the ground state energies of the different models. Up to now we only used the simple update to determine the TN approximation of the ground state. This method is very fast since it does not encompass the effects of the environment, but also not very accurate. A more accurate algorithm is the full update which is explained in the appendix A.1. This algorithm finds the tensor with a certain bond dimension which represents the absorption of a gate best, thus giving the best possible approximation. In addition to the different algorithm we will try to perform the calculations with a larger unit cell. This would ease up the strong restriction of translational invariance and hence give lower ground state energies.

Also, rather than to change the algorithms used, a different mapping between the kagome and the square lattice might lead to an improvement of the results. It might be that different mappings favour different kind of ground states, e.g. the combination of the up-triangles into one single site might favour the existence of a trimerized states (see appendix A.3). Especially in the spin-1 case this might improve the results by quite a margin since up to now we are not able to see any trimerization. This mapping of combining triangles in the kagome lattice would however result in a next-to-nearest neighbour interaction in the square lattice. We therefore would have to modify the used algorithms accordingly.

One other thing that could improve the results might be to choose different initial conditions. Within our code every calculation starts from random tensors. It is however possible that a different starting tensor leads to better final results. E.g. starting from a superposition of the ground states of the Heisenberg model on the triangular lattice should be a very good starting point, since the kagome lattice can be seen as a triangular lattice of triangles.

One of the main problems during this project was of course the limitation in terms of computational resources. One way to improve the computational requirements and the results is by implementing symmetries. One possibility would be to implement the $SU(2)$ or $U(1)$ symmetry in the algorithms which would result in a much lower effective physical dimension. This would enable us to perform calculations at higher bond dimensions which could additionally improve the results. This improvement has recently been shown in [34] with a code with implemented $SU(2)$ -symmetry.

Within the calculations of the different models not only the requirement of computational resources was very large, but also the needed

time to perform the calculations. Because of that it would be very useful to be able to calculate not only on CPUs but on GPUs. It is possible to convert the algorithms so that they are able to run on GPUs which would lead to a large speedup (the exact extend of the speedup is unknown but we expect it to be of a factor of roughly 2). This task is also set for the near future.

Part iv

APPENDIX

APPENDIX

A.1 THE FULL UPDATE

The full update is the optimal way to find the new tensors with a specific bond dimension D , after applying a given two-body operator. It is based on the minimization of the distance between the old and the new state. The distance δ itself is given by

$$\delta = \left\| |\Psi\rangle - |\tilde{\Psi}\rangle \right\|^2 = \langle \Psi | \Psi \rangle - \langle \Psi | \tilde{\Psi} \rangle - \langle \tilde{\Psi} | \Psi \rangle + \langle \tilde{\Psi} | \tilde{\Psi} \rangle \quad (\text{A.1})$$

where $|\Psi\rangle$ is the original state where the two-body gate is applied onto one single link and $|\tilde{\Psi}\rangle$ is the new state where the gate is already absorbed. The bond dimension of the new state $|\tilde{\Psi}\rangle$ however is the same as in $|\Psi\rangle$ (see fig. A.1). The distance itself can also be written in the form of a TN diagram. This is shown in figure A.2. If we fix now every tensor except one tensor A' and look for the minimum of this distance according to the variation of A' we get

$$\min_{A'} \left\| |\Psi\rangle - |\tilde{\Psi}\rangle \right\|^2 = \min_{A'} \left(\vec{A}'^\dagger \mathcal{N} \vec{A}' - \vec{A}'^\dagger \vec{\mathcal{M}} - \vec{\mathcal{M}}^\dagger \vec{A}' + \mathcal{C} \right) \quad (\text{A.2})$$

where \vec{A}' are all components of the tensor A' combined into one vector. $\vec{\mathcal{M}}$, \mathcal{N} and \mathcal{C} can be obtained as TN diagrams very easily by taking the corresponding tensor A' out of each of the four TN diagrams in figure A.2.

If we want to find the tensor A' which minimizes δ we must solve

$$\frac{\partial}{\partial \vec{A}'^\dagger} \left(\vec{A}'^\dagger \mathcal{N} \vec{A}' - \vec{A}'^\dagger \vec{\mathcal{M}} - \vec{\mathcal{M}}^\dagger \vec{A}' + \mathcal{C} \right) = 0 \quad (\text{A.3})$$

and we end up with

$$\mathcal{N} \vec{A}' = \vec{\mathcal{M}}. \quad (\text{A.4})$$

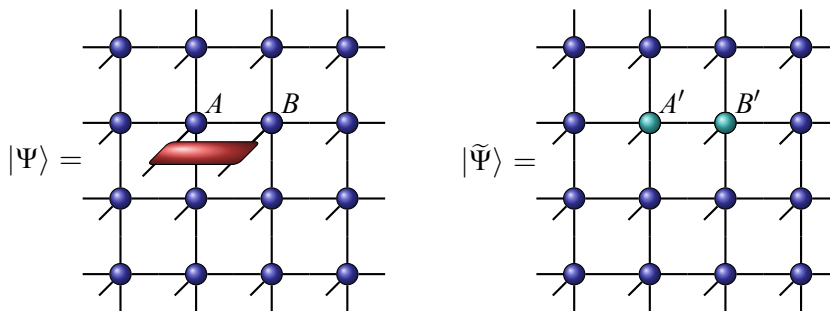


Figure A.1: Starting points of the full update

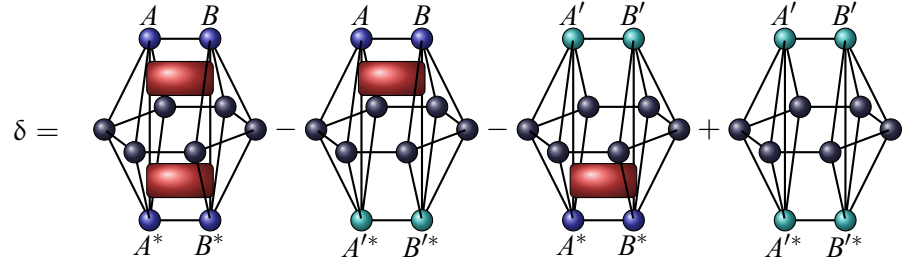


Figure A.2: Distance δ written as a TN. The outer blue and turquoise are the tensors which can also be seen in fig. A.1 and the darker ones correspond to some effective environment for these tensors

This problem can easily be solved by e.g. inverting the matrix \mathcal{N} . Now that we have obtained the first tensor which minimizes the distance, we fix A' and repeat every step for B' . In this way we iterate until we find the optimal tensors with bond dimension D which minimize the distance between $|\Psi\rangle$ and $|\tilde{\Psi}\rangle$. Thus we end up with the two tensors which represent the absorption of the two-body gate best. By performing a complete time step $U(\delta t)$ on the complete state we get a new TN state which now only consists of the new tensors A' and B' . To get to the ground state one has to repeat this process until both A' and B' have converged. To get faster convergence one usually does not start from random tensors but first performs the simple update to get tensors which are at least closer to the best approximated tensors than the random ones.

It is possible to improve the algorithm in terms of the computational cost by performing a SVD of the tensor, which should be updated. We perform the SVD between the link on which the gate is applied together with the physical link and all the other links which connect the tensor to the environment. From the resulting three tensors we absorb the tensor belonging to the environment into the environment and only update the remaining part. This scheme is more efficient in terms of the needed computational resources.

There are also very efficient ways to update the environment after each step by only absorbing the updated tensors once. This more efficient scheme, which is based on the same minimization of the distance, is described in more detail in [48].

A.2 CTM FOR A 2X2 UNIT CELL

From section 3.5.3.1 we know how to calculate the environment for a single tensor. Now we will extend this algorithm to a larger unit cell which consists of two different tensors. We therefore need the environment of a 2×2 unit cell and hence two more half-column and half-row tensors. This means that the effective environment is now given by $\mathcal{G}^{[r]} = \{C_1, T_{1a}, T_{1b}, C_2, T_{2a}, T_{2b}, C_3, T_{3a}, T_{3b}, C_4, T_{4a}, T_{4b}\}$.

Due to the increased amount of tensors within the environment we need a second truncation scheme for the links between the adjoining half-column or half-row tensors. For this truncation we use a similar scheme for the single tensor unit cell. We therefore combine each corner transfer matrix with the adjoining half-column and half-row tensor and the corresponding tensor of the unit cell into one large tensor Q . From this tensor we calculate a new isometry as before via $Q_1 Q_1^\dagger + Q_4 Q_4^\dagger = \tilde{W} \Lambda_W \tilde{W}^\dagger$. This new isometry will then be used to truncate the link between the half-row, or half-column tensors.

The complete scheme is displayed in the form of a TN in figure A.3

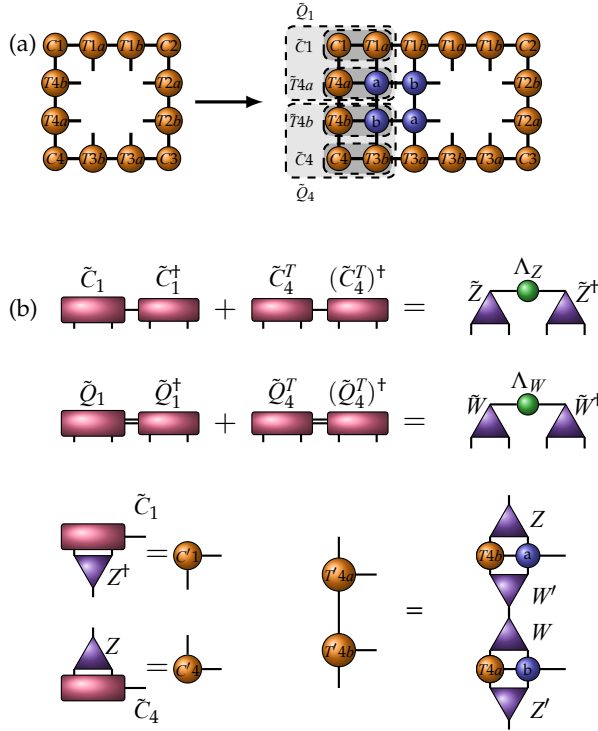


Figure A.3: Tensor network diagram of the CTM algorithm. In (a) a x-move is shown and (b) shows the renormalization scheme for the updated tensors.

A.3 DIFFERENT MAPPING FROM THE KAGOME TO THE SQUARE LATTICE

As explained in section 7.1, we have chosen a very specific mapping from the kagome to the square lattice. This mapping was chosen because the resulting interaction on the square lattice after the mapping is still local. Without the restriction of remaining with only a nearest-neighbour interaction on the square lattice it is possible to think of other mappings. As discussed in section 8.1, it might be that different mappings may favour different kind of ground states. We therefore want to discuss a different kind of mapping which may give better results especially in the case of the spin-1 KAFM.

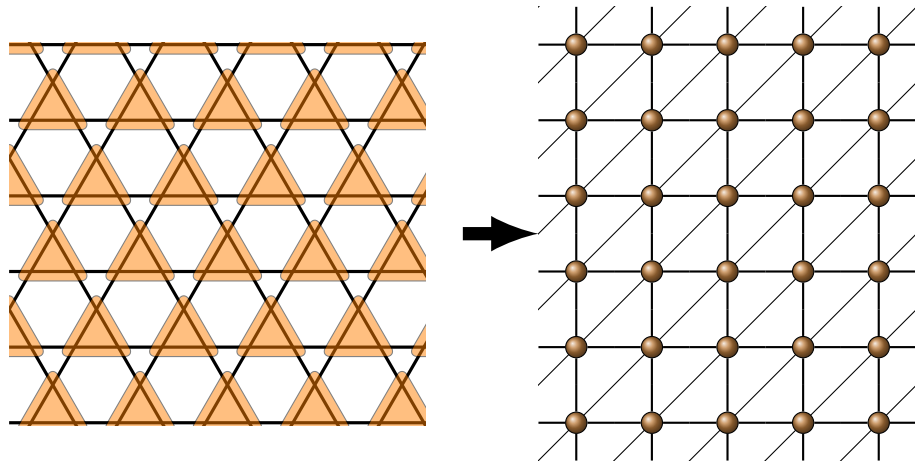


Figure A.4: Alternate mapping from the kagome to the square lattice. All up-triangles of the kagome are combined into one single site of the square lattice. This however results in a next-to-nearest neighbour interaction on the square lattice.

This mapping is done by combining all up-triangles of the kagome site into one single site of the square lattice. It therefore results in a next-to-nearest neighbour interaction on the square lattice (see fig. A.4) which is why it was not used in this thesis.

This mapping however is more likely to give rise to a trimerized ground state, as proposed for the ground state of the spin-1 KAFM. It is therefore expected that this kind of mapping would improve the results obtained for the spin-1 antiferromagnet on the kagome lattice.

BIBLIOGRAPHY

- [1] P.W. Anderson. Resonating valence bonds: A new kind of insulator? *Materials Research Bulletin*, 8:153–160, Feb 1973. doi: 10.1016/0025-5408(73)90167-0. (Cited on pages 43, 45, and 46.)
- [2] Alain Aspect, Philippe Grangier, and Gérard Roger. Experimental realization of einstein-podolsky-rosen-bohm *Gedankenexperiment* : A new violation of bell’s inequalities. *Phys. Rev. Lett.*, 49:91–94, Jul 1982. doi: 10.1103/PhysRevLett.49.91. URL <http://link.aps.org/doi/10.1103/PhysRevLett.49.91>. (Cited on pages 4 and 5.)
- [3] John S Bell et al. On the einstein-podolsky-rosen paradox. *Physics*, 1(3):195–200, 1964. (Cited on pages 3 and 5.)
- [4] Charles H. Bennett, Gilles Brassard, Claude Crépeau, Richard Jozsa, Asher Peres, and William K. Wootters. Teleporting an unknown quantum state via dual classical and einstein-podolsky-rosen channels. *Phys. Rev. Lett.*, 70:1895–1899, Mar 1993. doi: 10.1103/PhysRevLett.70.1895. URL <http://link.aps.org/doi/10.1103/PhysRevLett.70.1895>. (Cited on page 5.)
- [5] Henk WJ Blöte and Youjin Deng. Cluster monte carlo simulation of the transverse ising model. *Physical Review E*, 66(6):066110, 2002. (Cited on page 36.)
- [6] D. Bouwmeester, J. W. Pan, K. Mattle, M. Eibl, H. Weinfurter, and A. Zeilinger. Experimental quantum teleportation. *Nature*, 390: 575–579, 1997. (Cited on page 5.)
- [7] Sylvain Capponi, Oleg Derzhko, Andreas Honecker, Andreas M. Läuchli, and Johannes Richter. Numerical study of magnetization plateaus in the spin- $\frac{1}{2}$ kagome heisenberg antiferromagnet. *Phys. Rev. B*, 88:144416, Oct 2013. doi: 10.1103/PhysRevB.88.144416. URL <http://link.aps.org/doi/10.1103/PhysRevB.88.144416>. (Cited on pages 55 and 57.)
- [8] H. J. Changlani and A. M. Läuchli. Ground state of the spin-1 antiferromagnet on the kagome lattice. *ArXiv e-prints*, June 2014. (Cited on pages 59, 62, 63, and 64.)
- [9] Andrey Chubukov. Order from disorder in a kagomé antiferromagnet. *Phys. Rev. Lett.*, 69:832–835, Aug 1992. doi: 10.1103/PhysRevLett.69.832. URL <http://link.aps.org/doi/10.1103/PhysRevLett.69.832>. (Cited on page 67.)

- [10] J. I. Cirac, P. Zoller, H. J. Kimble, and H. Mabuchi. Quantum state transfer and entanglement distribution among distant nodes in a quantum network. *Phys. Rev. Lett.*, 78:3221–3224, Apr 1997. doi: 10.1103/PhysRevLett.78.3221. URL <http://link.aps.org/doi/10.1103/PhysRevLett.78.3221>. (Cited on page 5.)
- [11] M Cramer and J Eisert. Correlations, spectral gap and entanglement in harmonic quantum systems on generic lattices. *New Journal of Physics*, 8(5):71, 2006. URL <http://stacks.iop.org/1367-2630/8/i=5/a=071>. (Cited on page 11.)
- [12] Jane K. Cullum and Ralph A. Willoughby. *Lanczos algorithms for large symmetric eigenvalue computations. Vol. 1*, volume 41 of *Classics in Applied Mathematics*. Society for Industrial and Applied Mathematics (SIAM), Philadelphia, PA, 2002. ISBN 0-89871-523-7. (Cited on page 11.)
- [13] Sankar Das Sarma, Michael Freedman, and Chetan Nayak. Topologically protected qubits from a possible non-abelian fractional quantum hall state. *Phys. Rev. Lett.*, 94:166802, Apr 2005. doi: 10.1103/PhysRevLett.94.166802. URL <http://link.aps.org/doi/10.1103/PhysRevLett.94.166802>. (Cited on page 7.)
- [14] Stefan Depenbrock, Ian P. McCulloch, and Ulrich Schollwöck. Nature of the spin-liquid ground state of the $s = 1/2$ heisenberg model on the kagome lattice. *Phys. Rev. Lett.*, 109:067201, Aug 2012. doi: 10.1103/PhysRevLett.109.067201. URL <http://link.aps.org/doi/10.1103/PhysRevLett.109.067201>. (Cited on pages 45, 46, and 51.)
- [15] A. Einstein, B. Podolsky, and N. Rosen. Can quantum-mechanical description of physical reality be considered complete? *Phys. Rev.*, 47:777–780, May 1935. doi: 10.1103/PhysRev.47.777. URL <http://link.aps.org/doi/10.1103/PhysRev.47.777>. (Cited on pages 3 and 5.)
- [16] Artur K. Ekert. Quantum cryptography based on bell’s theorem. *Phys. Rev. Lett.*, 67:661–663, Aug 1991. doi: 10.1103/PhysRevLett.67.661. URL <http://link.aps.org/doi/10.1103/PhysRevLett.67.661>. (Cited on page 5.)
- [17] G. Evenbly and G. Vidal. Frustrated antiferromagnets with entanglement renormalization: Ground state of the spin- $\frac{1}{2}$ heisenberg model on a kagome lattice. *Phys. Rev. Lett.*, 104:187203, May 2010. doi: 10.1103/PhysRevLett.104.187203. URL <http://link.aps.org/doi/10.1103/PhysRevLett.104.187203>. (Cited on pages 45 and 51.)
- [18] Richard P. Feynman. Simulating physics with computers. *International Journal of Theoretical Physics*, 21(6-7):467–488, 1982. ISSN

- 0020-7748. doi: 10.1007/BF02650179. URL <http://dx.doi.org/10.1007/BF02650179>. (Cited on page 3.)
- [19] Danna E. Freedman, Robin Chisnell, Tyrel M. McQueen, Young S. Lee, Christophe Payen, and Daniel G. Nocera. Frustrated magnetism in the $s = 1$ kagome lattice $\text{BaNi}_3(\text{OH})_2(\text{VO}_4)_2$. *Chem. Commun.*, 48:64–66, 2012. doi: 10.1039/C1CC14731E. URL <http://dx.doi.org/10.1039/C1CC14731E>. (Cited on page 59.)
- [20] Y. Ge and J. Eisert. Area laws and efficient descriptions of quantum many-body states. *ArXiv e-prints*, November 2014. (Cited on page 12.)
- [21] O. Götze, D. J. J. Farnell, R. F. Bishop, P. H. Y. Li, and J. Richter. Heisenberg antiferromagnet on the kagome lattice with arbitrary spin: A higher-order coupled cluster treatment. *Phys. Rev. B*, 84:224428, Dec 2011. doi: 10.1103/PhysRevB.84.224428. URL <http://link.aps.org/doi/10.1103/PhysRevB.84.224428>. (Cited on pages 45, 51, 62, 67, 68, 70, and 76.)
- [22] I. S. Hagemann, Q. Huang, X. P. A. Gao, A. P. Ramirez, and R. J. Cava. Geometric magnetic frustration in $\text{Ba}_2\text{Sn}_2\text{Ga}_3\text{ZnCr}_7\text{O}_{22}$: A two-dimensional spinel based kagomé lattice. *Phys. Rev. Lett.*, 86:894–897, Jan 2001. doi: 10.1103/PhysRevLett.86.894. URL <http://link.aps.org/doi/10.1103/PhysRevLett.86.894>. (Cited on page 67.)
- [23] T.-H. Han, J.S. Helton, S. Chu, J.A. Nocera, D.G. andRodriguez-Rivera, C. Broholm, and Y.S. Lee. Fractionalized excitations in the spin-liquid state of a kagome-lattice antiferromagnet. *Nature*, 492:406–410, Dec 2012. doi: 10.1038/nature11659. (Cited on pages 45 and 46.)
- [24] Shigeo Hara, Hirohiko Sato, and Yasuo Narumi. Exotic magnetism of novel $s = 1$ kagome lattice antiferromagnet $\text{Kv}_3\text{Ge}_2\text{O}_9$. *Journal of the Physical Society of Japan*, 81(7):073707, 2012. doi: 10.1143/JPSJ.81.073707. URL <http://dx.doi.org/10.1143/JPSJ.81.073707>. (Cited on page 59.)
- [25] A. B. Harris, C. Kallin, and A. J. Berlinsky. Possible néel orderings of the kagomé antiferromagnet. *Phys. Rev. B*, 45:2899–2919, Feb 1992. doi: 10.1103/PhysRevB.45.2899. URL <http://link.aps.org/doi/10.1103/PhysRevB.45.2899>. (Cited on page 76.)
- [26] M. B. Hastings. Dirac structure, rvb, and goldstone modes in the kagomé antiferromagnet. *Phys. Rev. B*, 63:014413, Dec 2000. doi: 10.1103/PhysRevB.63.014413. URL <http://link.aps.org/doi/10.1103/PhysRevB.63.014413>. (Cited on page 45.)

- [27] H-X He, CJ Hamer, and J Oitmaa. High-temperature series expansions for the $(2+1)$ -dimensional ising model. *Journal of Physics A: Mathematical and General*, 23(10):1775, 1990. (Cited on page 36.)
- [28] K. Hida. Magnetization Process of the $S=1$ and $1/2$ Uniform and Distorted Kagomé Heisenberg Antiferromagnets. *Journal of the Physical Society of Japan*, 70:3673, December 2001. doi: 10.1143/JPSJ.70.3673. (Cited on pages 43, 55, 57, 64, and 65.)
- [29] Kazuo Hida. Ground state and elementary excitations of the $s=1$ kagomé heisenberg antiferromagnet. *Journal of the Physical Society of Japan*, 69(12):4003–4007, 2000. doi: 10.1143/JPSJ.69.4003. URL <http://dx.doi.org/10.1143/JPSJ.69.4003>. (Cited on pages 59, 62, and 64.)
- [30] Yasir Iqbal, Federico Becca, Sandro Sorella, and Didier Poilblanc. Gapless spin-liquid phase in the kagome spin- $\frac{1}{2}$ heisenberg antiferromagnet. *Phys. Rev. B*, 87:060405, Feb 2013. doi: 10.1103/PhysRevB.87.060405. URL <http://link.aps.org/doi/10.1103/PhysRevB.87.060405>. (Cited on pages 45 and 51.)
- [31] H Krauter, D Salart, CA Muschik, Jonas Meyer Petersen, Heng Shen, Thomas Fernholz, and Eugene Simon Polzik. Deterministic quantum teleportation between distant atomic objects. *Nature Physics*, 9(7):400–404, 2013. (Cited on page 5.)
- [32] Lieven De Lathauwer, Bart De Moor, and Joos Vandewalle. A multilinear singular value decomposition. *SIAM J. Matrix Anal. Appl.*, 21:1253–1278, 2000. (Cited on page 24.)
- [33] Wei Li, Shuo Yang, Meng Cheng, Zheng-Xin Liu, and Hong-Hao Tu. Topology and criticality in the resonating affleck-kennedy-lieb-tasaki loop spin liquid states. *Phys. Rev. B*, 89:174411, May 2014. doi: 10.1103/PhysRevB.89.174411. URL <http://link.aps.org/doi/10.1103/PhysRevB.89.174411>. (Cited on pages 59 and 62.)
- [34] Tao Liu, Wei Li, Andreas Weichselbaum, Jan von Delft, and Gang Su. Simplex valence-bond crystal in the spin-1 kagome heisenberg antiferromagnet. *Phys. Rev. B*, 91:060403, Feb 2015. doi: 10.1103/PhysRevB.91.060403. URL <http://link.aps.org/doi/10.1103/PhysRevB.91.060403>. (Cited on page 79.)
- [35] X.-S. Ma, T. Herbst, T. Scheidl, D. Wang, S. Kropatschek, W. Naylor, B. Wittmann, A. Mech, J. Kofler, E. Anisimova, V. Makarov, T. Jennewein, R. Ursin, and A. Zeilinger. Quantum teleportation over 143 kilometres using active feed-forward. *Nature*, 489:269–273, 2012. (Cited on page 5.)

- [36] JB Marston and C Zeng. Spin-peierls and spin-liquid phases of kagomé quantum antiferromagnets. *Journal of Applied Physics*, 69 (8):5962–5964, 1991. (Cited on page 45.)
- [37] N. D. Mermin and H. Wagner. Absence of ferromagnetism or antiferromagnetism in one- or two-dimensional isotropic heisenberg models. *Phys. Rev. Lett.*, 17:1133–1136, Nov 1966. doi: 10.1103/PhysRevLett.17.1133. URL <http://link.aps.org/doi/10.1103/PhysRevLett.17.1133>. (Cited on page 29.)
- [38] Seiji Miyashita. Magnetic properties of ising-like heisenberg antiferromagnets on the triangular lattice. *Journal of the Physical Society of Japan*, 55(10):3605–3617, 1986. doi: 10.1143/JPSJ.55.3605. URL <http://dx.doi.org/10.1143/JPSJ.55.3605>. (Cited on page 55.)
- [39] P. Nightingale and C.J. Umrigar. *Quantum Monte Carlo Methods in Physics and Chemistry*. C: [Nato ASI series. Springer Netherlands, 1999. ISBN 9780792355519. (Cited on pages 11 and 45.)
- [40] S. Nishimoto, N. Shibata, and C. Hotta. Controlling frustrated liquids and solids with an applied field in a kagome Heisenberg antiferromagnet. *Nature Communications*, 4:2287, August 2013. doi: 10.1038/ncomms3287. (Cited on pages 55 and 57.)
- [41] Picture of japanese basket. <http://iopscience.iop.org/0953-8984/19/14/140301>, Feb 2015. (Cited on page 44.)
- [42] J. Oitmaa, C. Hamer, and W. Zheng. *Series Expansion Methods for Strongly Interacting Lattice Models*. Cambridge University Press, 2006. ISBN 9780521842426. (Cited on page 11.)
- [43] Yoshihiko Okamoto, Masashi Tokunaga, Hiroyuki Yoshida, Akira Matsuo, Koichi Kindo, and Zenji Hiroi. Magnetization plateaus of the spin- $\frac{1}{2}$ kagome antiferromagnets volborthite and vesignieite. *Phys. Rev. B*, 83:180407, May 2011. doi: 10.1103/PhysRevB.83.180407. URL <http://link.aps.org/doi/10.1103/PhysRevB.83.180407>. (Cited on page 55.)
- [44] Koji Okuta, Shigeo Hara, Hirohiko Sato, Yasuo Narumi, and Koichi Kindo. Observation of $1/3$ magnetization-plateau-like anomaly in $s=3/2$ perfect kagomé lattice antiferromagnet $\text{KCr}_3(\text{OH})_6(\text{SO}_4)_2$ (cr-jarosite). *Journal of the Physical Society of Japan*, 80(6):063703, 2011. doi: 10.1143/JPSJ.80.063703. URL <http://dx.doi.org/10.1143/JPSJ.80.063703>. (Cited on pages 67, 71, and 72.)
- [45] Lars Onsager. Crystal statistics. i. a two-dimensional model with an order-disorder transition. *Phys. Rev.*, 65:117–149, Feb 1944. doi: 10.1103/PhysRev.65.117. URL <http://link.aps.org/doi/10.1103/PhysRev.65.117>. (Cited on pages 29 and 31.)

- [46] Román Orús. A practical introduction to tensor networks: Matrix product states and projected entangled pair states. *Annals of Physics*, 349(0):117 – 158, 2014. ISSN 0003-4916. doi: <http://dx.doi.org/10.1016/j.aop.2014.06.013>. URL <http://www.sciencedirect.com/science/article/pii/S0003491614001596>. (Cited on page 11.)
- [47] Román Orús and Guifré Vidal. Simulation of two-dimensional quantum systems on an infinite lattice revisited: Corner transfer matrix for tensor contraction. *Phys. Rev. B*, 80:094403, Sep 2009. doi: 10.1103/PhysRevB.80.094403. URL <http://link.aps.org/doi/10.1103/PhysRevB.80.094403>. (Cited on page 21.)
- [48] H. N. Phien, J. A. Bengua, H. D. Tuan, P. Corboz, and R. Orus. The iPEPS algorithm, improved: fast full update and gauge fixing. *ArXiv e-prints*, March 2015. (Cited on pages 19 and 84.)
- [49] T. Picot and D. Poilblanc. Nematic and supernematic phases in Kagome quantum antiferromagnets under a magnetic field. *ArXiv e-prints*, June 2014. (Cited on pages 59, 64, 65, and 68.)
- [50] Ying Ran, Michael Hermele, Patrick A. Lee, and Xiao-Gang Wen. Projected-wave-function study of the spin-1/2 heisenberg model on the kagomé lattice. *Phys. Rev. Lett.*, 98:117205, Mar 2007. doi: 10.1103/PhysRevLett.98.117205. URL <http://link.aps.org/doi/10.1103/PhysRevLett.98.117205>. (Cited on page 45.)
- [51] Subir Sachdev. Kagome- and triangular-lattice heisenberg antiferromagnets: Ordering from quantum fluctuations and quantum-disordered ground states with unconfined bosonic spinons. *Phys. Rev. B*, 45:12377–12396, Jun 1992. doi: 10.1103/PhysRevB.45.12377. URL <http://link.aps.org/doi/10.1103/PhysRevB.45.12377>. (Cited on page 67.)
- [52] Subir Sachdev. *Quantum Phase Transitions*. Cambridge University Press, second edition, 2011. ISBN 9780511973765. URL <http://dx.doi.org/10.1017/CB09780511973765>. Cambridge Books Online. (Cited on page 6.)
- [53] Rajiv R. P. Singh and David A. Huse. Triplet and singlet excitations in the valence bond crystal phase of the kagome lattice heisenberg model. *Phys. Rev. B*, 77:144415, Apr 2008. doi: 10.1103/PhysRevB.77.144415. URL <http://link.aps.org/doi/10.1103/PhysRevB.77.144415>. (Cited on pages 45 and 51.)
- [54] Masuo Suzuki. Generalized trotter’s formula and systematic approximants of exponential operators and inner derivations with applications to many-body problems. *Communications in Mathematical Physics*, 51(2):183–190, 1976. ISSN 0010-3616. doi: 10.1007/

- BF01609348. URL <http://dx.doi.org/10.1007/BF01609348>. (Cited on page 18.)
- [55] Brian Swingle. Entanglement renormalization and holography. *Phys. Rev. D*, 86:065007, Sep 2012. doi: 10.1103/PhysRevD.86.065007. URL <http://link.aps.org/doi/10.1103/PhysRevD.86.065007>. (Cited on page 3.)
- [56] Y. J. Uemura, A. Keren, K. Kojima, L. P. Le, G. M. Luke, W. D. Wu, Y. Ajiro, T. Asano, Y. Kuriyama, M. Mekata, H. Kikuchi, and K. Kakurai. Spin fluctuations in frustrated kagomé lattice system $\text{SrCr}_8\text{Ga}_4\text{O}_{19}$ studied by muon spin relaxation. *Phys. Rev. Lett.*, 73:3306–3309, Dec 1994. doi: 10.1103/PhysRevLett.73.3306. URL <http://link.aps.org/doi/10.1103/PhysRevLett.73.3306>. (Cited on page 67.)
- [57] Villain, J., Bidaux, R., Carton, J.-P., and Conte, R. Order as an effect of disorder. *J. Phys. France*, 41(11):1263–1272, 1980. doi: 10.1051/jphys:0198000410110126300. URL <http://dx.doi.org/10.1051/jphys:0198000410110126300>. (Cited on page 71.)
- [58] Fa Wang and Ashvin Vishwanath. Spin-liquid states on the triangular and kagomé lattices: A projective-symmetry-group analysis of schwinger boson states. *Phys. Rev. B*, 74:174423, Nov 2006. doi: 10.1103/PhysRevB.74.174423. URL <http://link.aps.org/doi/10.1103/PhysRevB.74.174423>. (Cited on page 45.)
- [59] Steven R. White. Density matrix formulation for quantum renormalization groups. *Phys. Rev. Lett.*, 69:2863–2866, Nov 1992. doi: 10.1103/PhysRevLett.69.2863. URL <http://link.aps.org/doi/10.1103/PhysRevLett.69.2863>. (Cited on page 4.)
- [60] Y. Xie, Z. J. Chen, F. Yu, J. X. Kong, B. Normand, and T. Xiang. Tensor renormalization of quantum many-body systems using projected entangled simplex states. *Phys. Rev. X*, 4:011025, Feb 2014. doi: 10.1103/PhysRevX.4.011025. URL <http://link.aps.org/doi/10.1103/PhysRevX.4.011025>. (Cited on pages 45 and 51.)
- [61] Z. Y. Xie, J. Chen, M. P. Qin, J. W. Zhu, L. P. Yang, and T. Xiang. Coarse-graining renormalization by higher-order singular value decomposition. *Phys. Rev. B*, 86:045139, Jul 2012. doi: 10.1103/PhysRevB.86.045139. URL <http://link.aps.org/doi/10.1103/PhysRevB.86.045139>. (Cited on page 23.)
- [62] Simeng Yan, David A. Huse, and Steven R. White. Spin-liquid ground state of the $s = 1/2$ kagome heisenberg antiferromagnet. *Science*, 332(6034):1173–1176, 2011. doi: 10.1126/science.1201080. URL <http://www.sciencemag.org/content/332/6034/1173.abstract>. (Cited on pages 45 and 51.)

- [63] Kun Yang, L. K. Warman, and S. M. Girvin. Possible spin-liquid states on the triangular and kagomé lattices. *Phys. Rev. Lett.*, 70:2641–2644, Apr 1993. doi: 10.1103/PhysRevLett.70.2641. URL <http://link.aps.org/doi/10.1103/PhysRevLett.70.2641>. (Cited on page 45.)
- [64] M. E. Zhitomirsky. Field-induced transitions in a kagomé antiferromagnet. *Phys. Rev. Lett.*, 88:057204, Jan 2002. doi: 10.1103/PhysRevLett.88.057204. URL <http://link.aps.org/doi/10.1103/PhysRevLett.88.057204>. (Cited on page 71.)